

CONFERENCES AND SYMPOSIA

PACS number: 01.10.Fv

Joint scientific session of the Physical Sciences Division of the Russian Academy of Sciences and the Joint Physical Society of the Russian Federation (30 November 2005)

A joint scientific session of the Physical Sciences Division of the Russian Academy of Sciences (RAS) and the Joint Physical Society of the Russian Federation was held in the Conference Hall of the P N Lebedev Physics Institute, RAS, on 30 November 2005. The following reports were presented at the session:

(1) **Kuznetsov V D** (N V Pushkov Institute of Terrestrial Magnetism, Ionosphere, and Radio Wave Propagation (IZMIRAN), RAS, Troitsk, Moscow region) "Heliophysics: from observations to models";

(2) **Zaitsev V V** (Institute of Applied Physics, RAS, Nizhnii Novgorod), **Stepanov A V** (Special Astronomical Observatory at Pulkovo (GAO), RAS, St.-Petersburg) "Problems of solar activity physics";

(3) **Churazov E M, Sunyaev R A, Sazonov S Yu, Revnivtsev M G** (Space Research Institute, RAS, Moscow), **Varshalovich D A** (A F Ioffe Physical-Technical Institute, RAS, St.-Petersburg) "Annihilation emission from the galactic center: the INTEGRAL observatory results";

(4) **Fabrika S N, Abolmasov P K, Karpov S V, Sholukhova O N** (Special Astrophysical Observatory (SAO), RAS, Nizhnii Arkhyz, Karachaevo-Cherkesiya Republic), **Ghosh K K** (Universities Space Research Association, NASA Marshall Space Flight Center, USA) "Ultraluminous X-ray sources in galaxies — microquasars or intermediate mass black holes".

An abridged version of the reports is given below.

PACS numbers: **96.60.–j**, 95.55.Ev, **95.75.–z**
DOI: 10.1070/PU2006v049n03ABEH005967

Heliophysics: from observations to models

V D Kuznetsov

1. Introduction

Modern heliophysics focuses on physical processes in the heliosphere, spanning from the solar interior to the boundary of the heliosphere at which the solar wind interacts with the interstellar medium forming the heliopause. Solar studies are important both for astrophysics and, as the Sun is the nearest star, for practical applications and for life itself on Earth. Modern solar and solar – terrestrial physics form virtually one science — heliophysics. As with many other branches of physics, heliophysical studies are based on a traditional scheme: from scientific equipment, through observations and experimental data gathering, to applications of theory and the construction of models of the phenomena observed.

Uspekhi Fizicheskikh Nauk **176** (3) 319 – 344 (2006)
Translated by K A Postnov; edited by A Radzig

2. Observations — experimental data

Lately, new and very important heliophysical results have been obtained mainly by space missions. Now, several heliophysical space missions are operating and providing researchers with experimental evidence. These include the NASA spacecrafts ULYSSES (launched in 1990), TRACE (Transition Region and Coronal Explorer) (1998), and RHESSI (The Reuven Ramaty High-Energy Solar Spectroscopic Imager) (2002), the ESA mission SOHO (Solar and Heliospheric Observatory), and the Russian – Ukrainian satellite CORONAS-F (Complex Orbital Circumterrestrial Solar Activity Observations) (2001); the last satellite stopped operating on December 6, 2005 due to natural orbit degradation.

The CORONAS-F satellite gathered rich observational data [1 – 3]. Its scientific payload included 15 instruments that observed the Sun throughout the entire electromagnetic spectrum, from optical to gamma-rays, so the satellite comprised a real heliophysical observatory. The diverse data obtained by this observatory allow us to make a thorough analysis of heliophysical phenomena. Principal scientific results of heliophysical studies, obtained by CORONAS-F in its last few years, were reported at the session of the Presidium of the RAS in January 2005 and are published in Refs [1 – 4].

3. Helioseismology

The nature of the 11-year solar cycle and solar activity phenomena is rooted in the solar interior. Thermonuclear reactions in the central regions of the Sun liberate energy that is transferred outwards through the radiative area and then by means of convective energy transport which is more effective when approaching the solar surface. The convective zone formed thus determines the dynamics of a magnetic field in the solar cycle. Information about the internal layers of the Sun can be collected by registering solar neutrino flux in ground-based observations [5] and by means of helioseismology when making satellite-based observations of global oscillations of the Sun as a gravitating plasma sphere [6].

The multichannel DIFOS spectrophotometer onboard the CORONAS-F satellite registered global oscillations (p-modes with periods of about 5 min) of the Sun by measuring tiny variations (10^{-6}) in the solar radiation flux

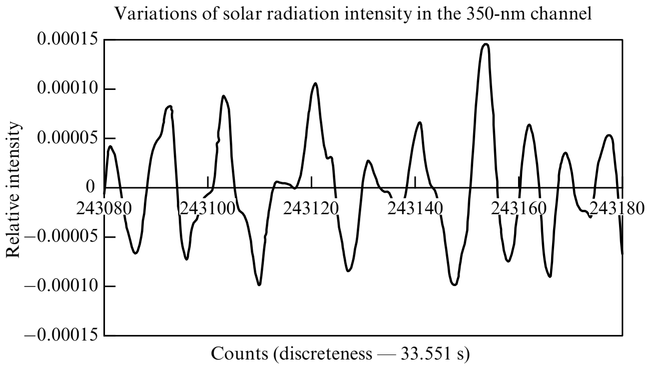

Figure 1. An example of the signal in the 350-nm channel of the DIFOS/CORONAS-F spectrophotometer, representing a set of harmonics with different periods, amplitudes, and phases, with a noise spectrum superimposed (the signal was cleaned from light reflected from the Earth's atmosphere).

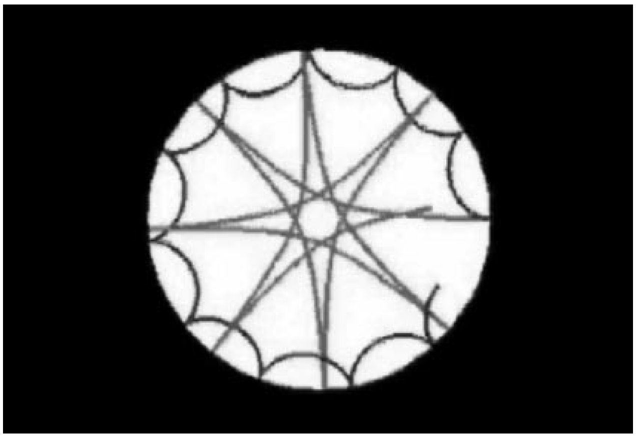

Figure 2. High and low spatial harmonics of global solar oscillations in the ray treatment. Shown is the propagation of a ray from the solar surface inward down to some critical radius where it is reflected back toward the surface, whence the ray is reflected inward again, thereby multiply propagating inside the Sun.

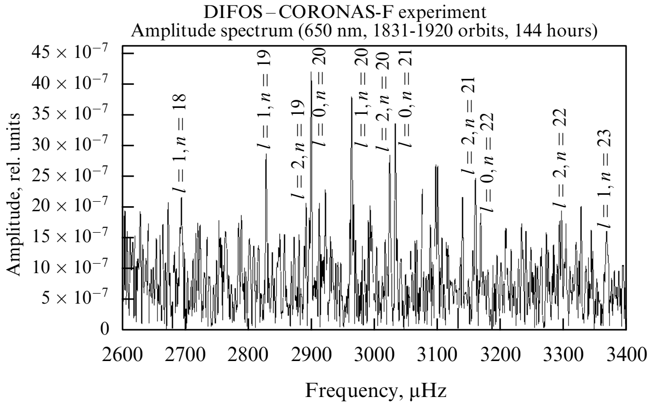

Figure 3. The amplitude spectrum of global solar oscillations reproduced from data obtained by the DIFOS/CORONAS-F instrument (IZMIRAN). Each peak corresponds to a global harmonic oscillation with a certain period (a harmonic). Numbers l and n characterize the number of nodes of the oscillation along the heliolongitude and the solar radius, respectively.

related to these oscillations over a wide wavelength range (350 – 1500 nm) [7]. Spectral analysis of optical signals received in eight spectral channels (Fig. 1) has been performed to find spectral harmonics with different periods, amplitudes, and phases. The device allows determination of low spatial harmonics of global oscillations (Fig. 2) (see also movie No. 1 in the electronic version of the paper on http://www.ufn.ru) (the number of nodes of an oscillation along the heliolongitude $l = 0, 1, 2$) that encompass all solar layers from the surface to the core. The resulting amplitude spectra of global oscillations (Fig. 3) show the presence of about 10 – 15 harmonics at each instant of time. Periods of individual harmonics as derived from these spectra allowed identification of the observed harmonics with the corresponding spatial ones of global solar oscillations (numbers l and n in Fig. 3). The coincidence of frequencies derived from observations with theoretically calculated ones allows verifying models of the internal structure of the Sun, for example, probing the convective zone depth. The frequencies coincide with high precision, allowing harmonics identification. An increasing measurement accuracy for periods of the harmonics and the refinement of their deviations from theoretically predicted values enable us to correct the model of the solar inner layers, which is one of the most important goals of helioseismology [6].

At some instant of time, the observed harmonics are randomly excited, persist for several days or weeks, then disappear and new harmonics with other periods emerge. Such a behavior can be explained by treating global oscillations as stochastically excited damping oscillations

$$\ddot{x}(t) + \gamma \dot{x}(t) + \omega^2 x(t) = \varepsilon(t)$$

with the exciting 'external force' $\varepsilon(t)$ determined by the action of the convective shell with a broadband noise spectrum on global oscillations resonating inside the Sun.

More fine effects related to the dependence of the frequency of harmonics on the solar cycle phase require long-term observations. Such series of observations were acquired by the DIFOS/CORONAS-F experiment (IZMIRAN) over four and a half years of monitoring at the activity decay phase of the current 23rd solar cycle, from its maximum in 2001 to December 2005. To provide the required accuracy of the spectral analysis, these data have been processed and 'cleaned' from the noise light reflected by the terrestrial atmosphere. Changes in the frequency of the harmonics with the cycle phase can be related to changes in the parameters of the solar internal structure model in use [8].

Broadband (350 – 1500 nm) observations revealed the global oscillations amplitude increasing toward UV wavelengths [3, 7]. These observations were confirmed by theoretical predictions — solutions of radiative magnetic hydrodynamic (MHD) equations in the radiation formation layers inside the photosphere [9, 10]. Theoretical spectral functions of the relative intensity fluctuations related to global oscillations fit the observed spectrum well. The established amplitude growth makes the UV channel the most appropriate for observations of global solar oscillations, which should be taken into account in planning future helioseismological experiments. These experiments will be continued with the 'Sokol' instrument (IZMIRAN) on board the third satellite of the CORONAS series, the CORONAS-FOTON, which is scheduled for launch in 2007 – 2008.

Radiation at various wavelengths (six different spectral channels of the DIFOS instrument: 350, 500, 650, 850, 1000, and 1500 nm) is observed as coming from different depths of the solar atmosphere, which allows (by performing simultaneous observations at these wavelengths) determination of the phases of global oscillation waves and studies of their propagation. The first attempts at such an analysis of the DIFOS/CORONAS-F experimental data were reported in Ref. [11].

A fine frequency analysis of spectra obtained in long-series observations makes it possible to determine the frequency splitting of harmonics due to the rotation of the Sun. This in turn provides the principal possibility of evaluating the angular rotational velocity of the solar inner layers [12]. The depth dependences of the angular velocity derived at different latitudes from the measurement data of the MDI (Michelson Doppler Imager) experiment on board SOHO [13] established the location of the tachocline region at the convective zone bottom, i.e., the turbulent mixing region formed by shear displacements at the depths characterized by a sharp variation of angular velocity gradient, where a solar dynamo operates and the magnetic field is amplified [14].

4. Emergence of magnetic fields and their fragmentation into magnetic tubes

Magnetic fields are thought to be primarily responsible for active phenomena on the Sun. The magnetic field is generated under the photosphere and emerges to the surface due to the magnetic buoyancy effect [15, 16] (see movie No. 2 in the electronic version of the paper on http://www.ufn.ru). When coming to the surface, as evidenced by numerous observations, the magnetic field is fragmented into flux tubes which mainly determine the structure and dynamics of the outer solar atmosphere.

By modeling subphotospheric layers of the Sun in the gravitational field by an exponential isothermal atmosphere with constant Alfvén velocity and being left over in the framework of MHD equations with turbulent viscosity, it is possible to reproduce the process of magnetic field decomposition into flux tubes and to determine their lateral and longitudinal sizes in terms of the maximum scales of the linear instability increment of magnetic buoyancy [17, 18]. For conditions in the convective zone (typical values of the turbulent viscosity $\nu_t = 1/3\nu l \approx 6\times10^{12}$ cm^2 s^{-1} as determined from the 'mixing length theory' and other parameters), the resultant magnetic tube sizes accord well with observed ones (lengthwise dimension 3×10^9 cm, lateral dimension 2×10^8 cm). In the solution obtained, the expression $\lambda_\perp \approx 2\pi(\nu_t u/g)^{1/2}$ (where u is the speed of sound, and g is the gravitational acceleration) for the lateral scale of the tubes is especially valuable, which has been obtained for the first time for a compressible medium using classical MHD approach. To an order of magnitude, this size is determined by the condition that the turbulent viscosity should have time to 'operate' over the characteristic time of magnetic buoyancy instability, which is determined in this case by the time of the sound propagation along the homogeneous atmosphere altitude (equal to u^2/g). The most suitable conditions for magnetic field fragmentation into tubes hold under the photosphere at depths of the hydrogen ionization zone (3×10^8 cm) where the adiabatic index of the gas, which determines its elasticity and resistance to the magnetic field line curvature, is minimal ($\gamma_{\min} = 1.09$).

The availability of magnetic flux buoyancy requires the finite superadaibaticity of convective zone, otherwise, by expanding according to the magnetic adiabatic law, magnetic clots can get cooler than the ambient medium and the magnetic buoyancy effect will be compensated. In the solar convective zone, the actual superadiabaticity is well above the calculated value of critical superadiabaticity:

$$\beta_\odot = \nabla T - \nabla_{\rm ad} T \approx 7\times10^{-9}\ \text{grad cm}^{-1} \gg \beta_{\rm crit} \approx 10^{-12}\ \text{grad cm}^{-1}\,,$$

i.e., the conditions for the positive magnetic buoyancy in the Sun are well satisfied. But, in principle, for stars with very feeble convection the situation is possible when the magnetic field emergence does not occur and hence there is no surface magnetic activity.

Many observations [19] allowed establishing the key role of buoyant magnetic fluxes in initiating flares and mass ejections. Here, one of the important parameters that determines the character of flaring and eruptive processes is the velocity of the flux rise to the corona; this velocity determines regimes of the magnetic reconnection and energy release in the current sheets, as well as the onset of the eruptive mass ejection instability (see Section 6).

The velocity of magnetic flux rise was estimated for average parameters from equating the magnetic buoyancy force (the analog of the Archimedes force) to the decelerating force on the assumption of mass and magnetic flux conservation for a clot, as well as its adiabatic (according to the magnetic adiabatic law) expansion [16]. In the convective zone, the decelerating force is due to the Stokes viscous force with the same value of the turbulent viscosity as we used when estimating magnetic tube scales (see above). When a clot comes from beneath the photosphere to the corona, where there is no more turbulence, the only force restricting the clot motion is the aerodynamic drag force. Thus, it becomes possible to justify the characteristic time of the magnetic field transport through the convective zone in the solar cycle, on the one hand, and to obtain the observed velocities of magnetic fluxes rising to the corona (not more than 1 km s^{-1}), as well as the observed direct dependence of the velocities on the strength of characteristic magnetic fields, on the other hand. So, good consistency of the model with observations may be achieved.

5. Current sheets and solar flares

Plasma conductivity in the solar corona is very high and as a consequence the magnetic field is 'frozen' into plasma. By interacting with coronal magnetic fields, new magnetic fluxes rising from beneath the photosphere (in the form of magnetic tubes and loops) form current sheets. The energy dissipation in these sheets leads to flares [20, 21] (see movie No. 3 in the electronic version of the paper on http://www.ufn.ru). The analysis of extensive observational data with high spatial resolution, obtained over the last few years by the TRACE and SOHO satellites [19], gives compelling evidence that solar flares preferentially occur exactly in regions of a new buoyant magnetic field. This fact strongly confirms once again the concept developed by S I Syrovatskii and his disciples that current sheets and magnetic reconnection are the principal physical factors responsible for flaring energy release (see, for example, Refs [20, 22, 23]). It also serves as the physical basis for developing the methods of solar flare prognosis now providing a 90% accuracy from observations of magnetic fields and their associated currents [24]. The build-up of currents that emerge from the interaction of buoyant magnetic fields and lead to flares starts at around 10–30 hours before a flare and depends on the velocity of the rising flux tube and the magnetic field strength [25, 26].

Current sheets are formed on zero (in general, separatrix) magnetic field lines that can be localized from the magnetic field distribution at the photospheric level where measured data are available for the magnetic fields [27]. Even the greatly simplified but typical flare activity model in which a fresh magnetic flux rising into an already existing active region with a weak background magnetic field (which is always present) gives birth to many zero points. The localization of these points topologically changes depending on the field strength. They fall either on open or closed field lines, which largely determines the dynamics of particles accelerated in flares and their escape to the interplanetary space [28]. The three-dimensional magnetic field of an active region represents a continuous magnetic carpet [29] (see movie No. 4 in the electronic version of the paper on http://www.ufn.ru) and comprises many zero points and lines, separatrix and singular surfaces on which current sheets are produced and the magnetic reconnection occurs. The latter provides a redistribution of magnetic fields between interacting magnetic fluxes.

Rather many mechanisms have been proposed for describing instabilities and the destruction of current sheets that cause rapid release of stored magnetic energy [21]. The energy accumulation in a sheet occurs with an increase of current that heats up plasma and leads to the production of nonthermal particles. Using equations of anisotropic (collisionless) MHD [30] made it possible to establish that a fairly small admixture of hot ions with positive temperature anisotropy ($A = T_{\perp,\mathrm{h}}/T_{\parallel,\mathrm{h}} - 1 \approx 0.5$), corresponding to real conditions in a current sheet, is capable of initiating the passage to the fast reconnection regime (the increment $\gamma L/V_{A,\mathrm{i}} \geqslant 0.1$). When the number density of these particles (ions) reaches some threshold value (for typical conditions in the corona it is about 0.02 of the background particle number density), an anisotropic instability develops in the sheet (the analog to the Weibel instability for Alfvén type perturbations), initiating the fast reconnection regime with the characteristic Alfvén velocities. Therefore, due to this instability current sheets are 'doomed' to be destroyed when the current increases and critical conditions are reached.

Superimposing hard X-ray and hard UV images simultaneously obtained by the TRACE and RHESSI space missions allowed localization of the flaring energy release and proved that it is related to the current sheet and magnetic reconnections inside it [31] (see movie No. 5 in the electronic version of the paper on http://www.ufn.ru).

6. Mass ejections

Emerging twisted magnetic loops are injected from the corona into the interplanetary space in the form of so-called coronal mass ejections [32, 33]. These are the largest-scale and most powerful solar activity phenomena (Fig. 4) (see also movie No. 6 in the electronic version of the paper on http://www.ufn.ru). Many observations show [32] that the slow evolution of magnetic configurations (loops, arches) in the Sun is followed by the loss of equilibrium and in most cases mass ejections represent twisted magnetic loops. Twisting of

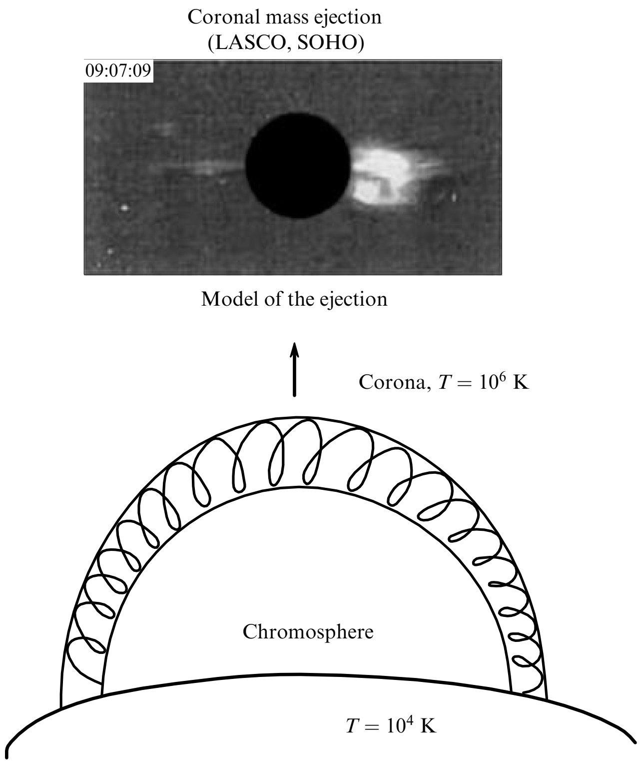

Figure 4. A coronal mass ejection in the form of a twisted loop.

the loops is observed both in the Sun during the eruption itself in the corona, as evidenced by observations made with the Yohkoh and TRACE spacecrafts [34] (see movie No. 7 in the electronic version of the paper on http://www.ufn.ru), and in the interplanetary space, as measured by other space missions. The loop strongly expands by preserving its connection to the Sun [35].

The eruptive instability of emerging twisted magnetic loops can be understood in terms of quasistationary MHD evolution [36] which proceeds in its development through a sequence of equilibrium states of an emerging twisted magnetic tube in the solar atmosphere. On the other hand, the disturbance of equilibrium and setting in of the dynamical phase (i.e., the necessity of taking into account the velocity terms in MHD equations) is related to the absence of (quasistationary) solutions for some conditions (at some critical altitude in the solar atmosphere in this case).

Using the Gold and Hoyle type twisted magnetic field for the model [37] and modifying it by the gas pressure inside the tube, and also assuming tube equilibrium with the ambient plasma (the equality of total pressures at the boundary), as well as the conservation of mass and longitudinal magnetic flux in the tube, it is possible to establish [37, 38] that the growth of twistedness of a magnetic field in the tube, as it slowly rises and expands (in the solar atmosphere with pressure decreasing with height), at a certain altitude reaches some critical value corresponding to the onset of developing kink instability. This instability leads to energy dissipation from the twisted magnetic field component and the heating of plasma in the tube. In the framework of quasistationary approximation, the phenomenological account for such heating in the flux tube equation, which represents a unique and monotonic dependence of the tube's equilibrium radius on the altitude in the solar atmosphere, reduces to introducing a temperature dependence in the rising flux tube on its

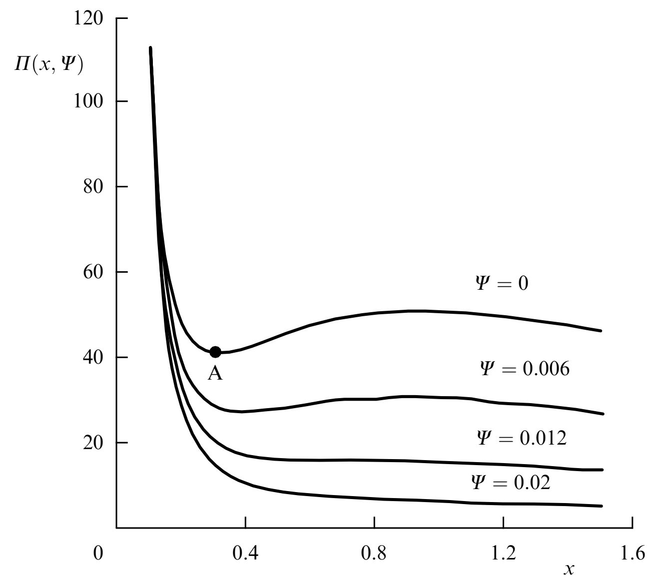

Figure 5. The total pressure $\Pi(x)$ in the flux tube as a function of the dimensionless radius [or the altitude h in the solar atmosphere, $x = x(h)$] for different values of the dimensional parameter Ψ characterizing the ratio of the mass outflow velocity to the flux tube rise speed. The point A corresponds to loss in tube equilibrium.

radius (or the altitude in the solar atmosphere, which is equivalent). This changes the tube equation itself and leads to the appearance of a point A in the 'tube radius – altitude' dependence (Fig. 5), at which the monotonic (quasistationary) solution disappears, and, hence, small changes in the tube altitude in the solar atmosphere should correspond to finite changes in its radius, which is only possible for finite velocities, i.e., the solution is no longer quasistationary. This signals the occurrence of the dynamical phase — rapid flux tube expansion. The density in the tube also rapidly decreases, and due to the emerging impulse buoyancy force the tube is abruptly pushed upwards into more rarefied layers of the corona. The tube occupies there a new quasistationary equilibrium state and is perceived as a mass excess, which is the actual mass ejection observed.

The physical meaning of the appearance of point A in the curve shown in Fig. 5 is related to the increase in magnetic tube twistedness and the associated energy dissipation, heating, and pressure in the tube as it rises and expands sideways, while the pressure in the solar atmosphere decreases with altitude, which leads (in the framework of quasistationary MHD evolution) to the 'nonequilibrium point', analogous to the theory of catastrophes.

In the place of an ejected loop, a rarefaction emerges, which appears as a darkening because the plasma mass and emission measure decrease. These darkenings have been observed many times by the solar X-ray telescope on board the CORONAS-F satellite, for example, during a period of very powerful events in October 2003 [1, 3] (see movie No. 8 in the electronic version of the paper on http://www.ufn.ru).

If a loop rises slowly, the mass outflow through its ends should be taken into account. This results in the total pressure decreasing in the tube, which can suppress the eruptive instability under certain conditions.

The mass loss with constant outflow velocity is proportional to the mass itself, so an exponential term appears in the equation for the pressure in the tube. Numerical solutions of the transcendental equation for different values of the dimensionless parameter Ψ involved that characterizes the ratio of the mass outflow velocity to the tube rise velocity are shown in Fig. 5. When the dimensionless parameter Ψ exceeds some critical value (0.012 in this case), the nonequilibrium point A disappears. The inflexion point of the curve is critical, where both the first and second derivatives vanish. At this point, the radius of the tube increases 2.6 times with respect to its value at the beginning of outflow, the tube loses most of its mass, and the minimal ejection mass is 0.28 times the initial mass of the tube. The model-based injection altitudes of the flux tube and all its parameters at the moment of injection (the total mass, the magnetic flux) correspond well to observed values.

Thus, in this model the mass ejection and the setting in of eruption instability are related to each other: flux tubes losing a lot of mass (during a slow rise) are stable against the eruptive instability, while those losing little mass (during a rapid rise), in contrast, are subject to the eruptive instability that effects the mass ejection. As noted in Section 4, the elevating velocity of buoyant magnetic fluxes is directly proportional to the magnetic field strength that ultimately determines the development of events.

7. Heliopause

The solar wind, disturbances, and mass ejections extend over the heliosphere, interact with planetary magnetospheres, and ultimately reach the heliospheric boundary — the heliopause that results from the interaction of the solar wind with the interstellar medium at around 100 AU from the Sun. Two shock waves are generated on each side of the heliopause. One of them retards the incoming flow of supersonic interstellar gas, the other retards the solar wind supersonic flow. After crossing these shocks, the colliding media form the heliopause separating the solar wind and the interstellar medium.

The Voyager-1 and Voyager-2 spacecrafts, which were launched in 1977 and are now investigating the outer heliosphere, have already approached its putative boundary. The first measurement data obtained from Voyager-1 that crossed the internal shock showed the presence of a spatial anisotropy of particles, a jump in the magnetic field strength and other features in the medium parameters [39]. Additional information is expected to come soon when Voyager-2 will cross the heliospheric boundary.

The state of the heliopause as a tangential MHD discontinuity is determined by its stability or instability with respect to disturbances in the medium that forms it. The exchange between the heliosphere and the bounding interstellar medium, in particular, the penetration of interstellar hydrogen into the heliosphere and the formation of chemical composition of the heliosphere, also depends on this state. This problem is actively discussed in the literature [41].

We studied the dependence of the heliopause stability on the characteristics of the forming medium by modeling the heliopause as a plane tangential discontinuity separating the magnetized interstellar plasma and nonmagnetized solar wind plasma in the anisotropic MHD approximation [42]. Figure 6 depicts the model-produced dependence of the threshold Mach number at which the modified (by 'hose' anisotropic instability) Kelvin – Helmholtz instability of the heliopause occurs as a function of the plasma temperature anisotropy $D = 1 - T_{\parallel}/T_{\perp}$. Such an anisotropy can be tied up with nearby shocks. The critical Mach number in the

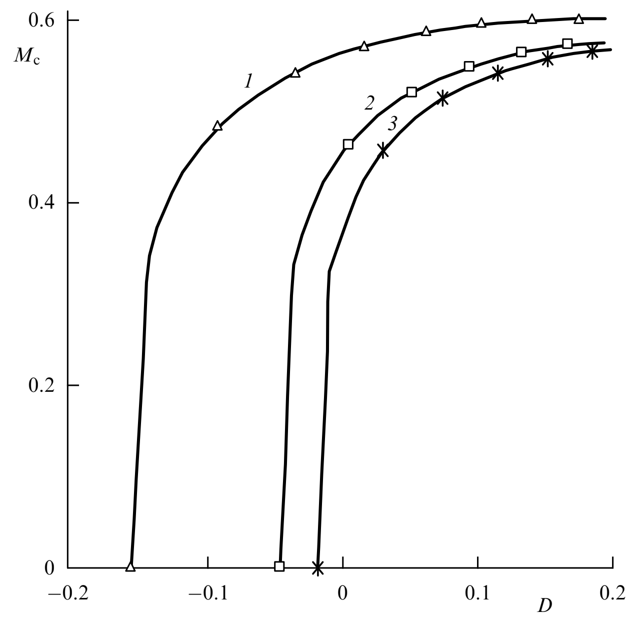

Figure 6. The critical Mach number (M_c) corresponding to the Kelvin – Helmholtz instability threshold as a function of the temperature anisotropy degree D. Curve *1* corresponds to $\beta = 0.05$, *2* — 0.03, and *3* — 0.02; β is the kinetic-to-magnetic pressure ratio. Regions above the curves are unstable.

isotropic case is $M = 0.45$. It is seen that in the anisotropic case the instability is possible at smaller Mach numbers, and the dependence itself of the threshold Mach number on the degree of anisotropy is very sharp in character. The zero critical Mach numbers correspond to purely anisotropic 'hose' instability that sets in at small anisotropies (5 – 15%). Thus, the heliopause is characterized by a high instability with respect to parameters of the medium that forms it and so can reside in a diffusive turbulent state. This should be born in mind when interpreting measurements to be carried out by the Voyager-1 and Voyager-2 spacecrafts.

8. Future heliophysical space projects

Getting new heliophysical data capable of stimulating the development of new models and providing better understanding of physical processes occurring in the Sun and in the heliosphere is related to future space missions that are being developed and prepared by space agencies in different countries.

Modern heliophysical space studies focus on obtaining images with high spatial resolution [as in the NASA projects TRACE, SDO (Solar Dynamic Observatory)], performing local measurements in several spatially separated points (the NASA project SENTILIES) and near the Sun (the NASA project 'Solar Probe', the RAS and Roskosmos project 'Interheliozond'), and carrying out stereo observations of the Sun [the NASA project STEREO (Solar Terrestrial Relations Observatory)]. Numerical simulation of the heliophysical processes using data obtained from space observatories should also play a significant role.

Within the framework of the Federal Space Program, IZMIRAN together with the Space Research Institute (IKI), RAS are working on the heliophysical project 'Interheliozond' [43, 44], which envisages performing new original observations that become possible due to the proposed heliocentric orbit of the spacecraft. The spacecraft will start from the Earth and after a large series of gravitational maneuvers near Venus will approach the Sun by a distance of up to 30 solar radii. The gravitational maneuvering near Venus also makes it possible to incline the spacecraft orbit to the ecliptical plane.

Such a heliocentric orbit, where the spacecraft having approached the Sun will go out of the ecliptical plane and take different positions relative to the Sun – Earth line, allows:

• observing small scales in the Sun, which is a prerequisite to studying the fine structure and dynamics of the solar atmosphere — the magnetic network, magnetic elements, turbulence — as well as to investigating supergranulation and magnetic loops in microflares and reconnection;

• carrying out observations of the Sun and local measurements in the regime of spacecraft corotation with solar rotation, which is important when studying spatial and temporal links between local characteristics of the solar wind, energetic particles and magnetic fields in the heliosphere and their sources in the Sun and coronal structures;

• performing local measurements near the Sun, which are necessary for investigating mechanisms of the solar corona heating and solar wind acceleration, the nature of turbulence and particle acceleration;

• executing out-of-ecliptical observations of the Sun and its poles, the ecliptical corona and the coronal streamer belt, and the heliolongitudinal extent of mass ejections;

• realizing stereoscopic observations of the Sun in cooperation with ground-based and circumterrestrial observations.

9. Conclusion

Modern heliophysics is a very broad and deep science with many researchers involved in its advancement. The present communication reports on the results obtained by the author in this field and does not pretend to be a comprehensive review of modern heliophysics. Recently, a lot of interest in heliophysics has been related to its applications, so-called space weather — effects of solar activity on the Earth and various aspects of human activities on the Earth and in space. It is important that the results of fundamental research ultimately underlay space weather forecasting, and the task of heliophysicists is to extend this knowledge on the basis of observations, theory, and modeling.

References

1. Kuznetsov V D, Zhitnik I A, Sobel'man I I *Vestn. Ross. Akad. Nauk* **75** 704 (2005) [*Herald Russ. Acad. Sci.* **75** 370 (2005)]
2. Kuznetsov V D *COSPAR Inform. Bull.* **161** 90 (2004)
3. Kuznetsov V D *Astron. Vestn.* **39** 485 (2005) [*Solar Syst. Res.* **39** 431 (2005)]
4. Kuznetsov V D *Izv. Ross. Akad. Nauk Ser. Fiz.* **70** 58 (2006)
5. Fukuda Y et al. *Phys. Rev. Lett.* **77** 1683 (1996)
6. Christiansen-Dalgaard J, in *Lecture Notes on Stellar Oscillations* (Danmarks: Inst. Fys. Astron., 2003) p. 5
7. Lebedev N I et al. *Astron. Zh.* **81** 956 (2004) [*Astron. Rep.* **48** 871 (2004)]
8. Howe R et al. *Astrophys. J.* **588** 1204 (2003)
9. Zhugzhda Y D, Staude J, Bartling G *Astron. Astrophys.* **305** L33 (1996)
10. Dzhalilov N S, Shtaude Yu *Global'nye Kolebaniya Solntsa* (Global Oscillations of the Sun) (Baku – Moscow: Elm, 2005) p. 25
11. Zhugzhda Yu D *Pis'ma Astron. Zh.* **32** 366 (2006)
12. Hasler K-H et al. *Astron. Astrophys.* **322** L41 (1997)

13. Kosovichev A G et al., in *Sounding Solar Stellar Interiors*: *Proc. of the 181st Symp. of Intern. Astron. Union, Nice, France, September 30–October 3, 1996* (Eds J Provost, F-X Schmider) (Dordrecht: Kluwer Acad. Publ., 1997) p. 203
14. Spiegel E A, Zahn J-P *Astron. Astrophys.* **265** 106 (1992)
15. Parker E N *Cosmical Magnetic Fields*: *Their Origin and Their Activity* (Oxford: Clarendon Press, 1979) [Translated into Russian: Vol. 1 (Moscow: Mir, 1982) p. 412]
16. Kuznetsov V D, Syrovatskii S I *Astron. Zh.* **56** 1263 (1979) [*Sov. Astron.* **23** 715 (1979)]
17. Kuznetsov V D *Magnitnaya Gidrodinamika* **2** 13 (1987)
18. Kuznetsov V D, in *Physics of Magnetic Flux Ropes* (Geophys. Monograph, Vol. 58, Eds C T Russell, E R Priest, L C Lee) (Washington, DC: American Geophys. Union, 1990) p. 77
19. Schrijver C J et al. *Astrophys. J.* **628** 501 (2005)
20. Syrovatskii S I, Bulanov S V, Dogel' V A "Fizika solnechnykh vspyshek" ("Physics of solar flares"), in *Itogi Nauki i Tekhniki Ser. Astronomiya* (Progress in Science and Technology. Ser. Astronomy) Vol. 21 (Moscow: VINITI, 1982) p. 188
21. Priest E, Forbes T *Magnetic Reconnection*: *MHD Theory and Applications* (Cambridge: Cambridge Univ. Press, 2000) [Translated into Russian (Moscow: Fizmatlit, 2005) p. 352]
22. Kuznetsov V D, Syrovatskii S I *Solar Phys.* **69** 361 (1981)
23. Kuznetsov V D *Astron. Zh.* **59** 108 (1982) [*Sov. Astron.* **26** 67 (1982)]
24. *Space News* **16** (33) 16 (2005); *Raketnaya Kosmicheskaya Tekh.* (TsNIIMASh) (41) 2 (2005)
25. Syrovatskii S I *Pis'ma Astron. Zh.* **2** 35 (1976) [*Sov. Astron. Lett.* **2** 13 (1976)]
26. Heyvaerts J, Priest E R, Rust D M *Astrophys. J.* **216** 123 (1977)
27. Schmieder B et al. *Solar Phys.* **150** 199 (1994)
28. Kuznetsov V D *Solnechnye Dannye* (Bull.) (7) 83 (1985)
29. Priest E R, Heyvaerts J F, Title A M *Astrophys. J.* **576** 533 (2002)
30. Gamayunov K V, Oraevsky V N, Kuznetsov V D *Plasma Phys. Control. Fusion* **40** 1285 (1998)
31. Saint-Hilaire P, Benz A O *Solar Phys.* **210** 287 (2002)
32. Kuznetsov V D, in *Itogi Nauki i Tekhniki Ser. Astronomiya* (Progress in Science and Technology. Ser. Astronomy) Vol. 45 (Moscow: Kosmosinform, 1994) p. 3
33. Dere K P, Wang J, Yan Y (Eds) *Coronal and Stellar Mass Ejections*: *Proc. IAU Symp.* No. 226 (Cambridge: Cambridge Univ. Press, 2005)
34. Leka K D et al. *Astrophys. J.* **462** 547 (1996)
35. Burlaga L F *Planet. Space Sci.* **49** 1619 (2001)
36. Priest E R *Solar Magnetohydrodynamics* (Dordrecht: D. Reidel Publ. Co., 1984) [Translated into Russian (Moscow: Mir, 1985) p. 189]
37. Kuznetsov V D, Hood A W *Solar Phys.* **171** 61 (1997)
38. Kuznetsov V D, Hood A W *Adv. Space Res.* **26** 539 (2000)
39. Burlaga L F et al. *Science* **309** 2027 (2005)
40. Jokipii J R, Giacalone J *Astrophys. J.* **605** L145 (2004)
41. Baranov V B, Fahr H J *J. Geophys. Res.* (*Space Phys.*) **108** (A3) 1110 (2003)
42. Kuznetsov V D, Nakaryakov V M, Tsyganov P V *Pis'ma Astron. Zh.* **21** 793 (1995) [*Astron. Lett.* **21** 710 (1995)]
43. Marsch E et al., in *Proc. of the Conf. Crossroads for European Solar and Heliospheric Space Physics, Puerto de la Cruz, Tenerife, Spain, March 23–27, 1998* (ESA SP, No. 417, Eds E R Priest, F Moreno-Insertis, R A Harris) (Noordwijk, The Netherlands: ESA Publ. Division, 1998) p. 91
44. Kuznetsov V D *Zemlya Vselennaya* (2) 18 (2000)

PACS numbers: **96.60.–j**, 96.60.Pb, 97.10.Jb
DOI: 10.1070/PU2006v049n03ABEH005968

Problems of solar activity physics

V V Zaitsev, A V Stepanov

1. Introduction

The energy emitted by the Sun ('the solar luminosity', 3.86×10^{26} W) determines almost all processes on the Earth. Although the solar bolometric luminosity is 3–4 orders of magnitude higher than the power of flares and solar ejections of matter, it is these phenomena that have a significant impact on the situation in the circumterrestrial space, ionosphere, and the terrestrial atmosphere. Solar flares are accompanied by plasma heating, charged particle acceleration, eruptive phenomena and electromagnetic energy generation in a wide wavelength range from the gamma-rays to radio band, and most completely reflect the concept of a solar activity.

In 2007, under the auspices of the United Nations Organization, the scientific program International Heliophysical Year (IHY) will begin. This program, like the program International Geophysical Year executed 50 years ago, should join efforts of solar researchers and geophysicists from around the world to formulate and solve important problems concerning the origin of solar activity, the prognosis of active solar phenomena, and their impact on the Earth.

In this report we discuss actual problems of the physics of solar flares, which include mechanisms of flaring energy release; mechanisms of charged particle acceleration and features of their propagation, and the problem of flaring plasma diagnostics. Prospects for solving these problems are illustrated by the example of coronal magnetic arches — fundamental structures in the solar atmosphere and in flare stars.

2. The origin of a flare. Equivalent electric circuit

Most likely, there is no universal mechanism for describing different features of solar flares (C de Jager: "*Flares are different*"). More than ten models and their modifications are being discussed in the current literature. A developed solar flare possesses a complex magnetic configuration consisting of a set of arches (loops) with a characteristic size of $10^9 - 10^{10}$ cm. Such a structure is also observed in late-type stars. The most popular current models comprise the model of interacting magnetic loops [1, 2]; flares in the coronal streamer [3]; the model with outgoing magnetic flux [4]; 'statistical' flares [5], and models of single flare loops [6, 7]. These models, as a rule, invoke the mechanism of 'reconnection' of magnetic field lines, studied by Syrovatskii [8] and Somov [9].

The 'electric circuit' model proposed by Alfvén and Carlqvist [10] is based on measurements made by Severnyi (see Ref. [11]), who discovered electric currents $I \geqslant 10^{11}$ A in the vicinity of solar spots, and on the analogy to a circuit with mercury rectifier capable of producing a sharp transition from a high-conductivity state to that with a great resistance. At the instant of breaking the current in the circuit, an explosive energy release occurs. It is crucial to understand the mechanisms of the current 'breaking'. By developing the model [10], we accounted for the following: (1) a flare is principally a nonstationary process, so that the stationary Ohm law $\mathbf{j} = \sigma \mathbf{E}$ is inapplicable for describing the flare, and (2) the neutral plasma component plays a decisive role in the electric current energy dissipation.

2.1 The model of a single loop flare with current

Data from optical, X-ray (SMM, Yohkoh, TRACE, RHESSI, CORONAS-F) and radio observations (VLA, NoRH, SSRT) indicate that quite frequently solar flares are registered as occurring in isolated arches (single loop flares)

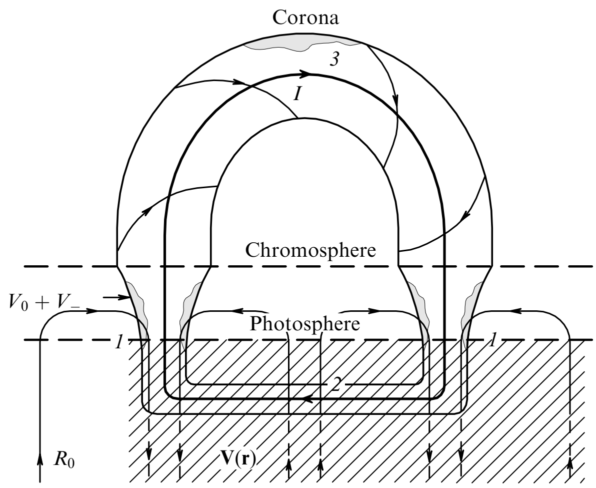

Figure 1. Schematic of a coronal magnetic loop formed by the convergent convective fluxes of photospheric plasma. $\mathbf{V}(\mathbf{r})$ is the matter velocity.

located far away from solar spots [7, 11]. Let us consider electrodynamical processes occurring in single flare loops, which is important both for the interpretation of single arches and for the understanding of the physics of flares with a complex magnetic structure.

Simple estimates [12, 13] show that the electric current energy stored in an arch, $W = LI^2/2$, with a magnetic arch's inductivity $L \sim 10$ H and current $I \sim 10^{11} - 10^{12}$ A amounts to $5 \times 10^{22} - 5 \times 10^{24}$ J, which is sufficient for a solar flare. However, the power released at classical (Spitzer) resistance of the arch $R \sim 10^{-11}\ \Omega$ is around $\mathrm{d}W/\mathrm{d}t = RI^2 \sim 10^{11} - 10^{13}$ W, which is 8–10 orders of magnitude smaller than that of a solar flare. The flare will occur if the resistance increases up to $10^{-4} - 10^{-2}\ \Omega$, which is equivalent to current breaking. The reason for the significant increase in the circuit resistance is one of the main problems in the theory of flares. The 'electric circuit' model was further developed in Refs [12–18].

Figure 1 displays a magnetic loop rooted in the photosphere, whose footpoints are formed by converging fluxes of photospheric matter. Such a situation occurs when the footpoints of the loop are located at the nodes of several supergranulation cells. The existence of strong electric currents in coronal arches is confirmed by observations [19] and the TRACE data that suggest a virtually constant cross section of the arch along its length, which is unlikely for a potential magnetic field. In this structure, three regions can be separated.

In region 1 located in the photosphere, a magnetic field with associated consistent electric current is generated. In this region, $\omega_e/\nu_{ea} \gg 1$, $\omega_i/\nu_{ia} \ll 1$, where ω_e and ω_i are gyrofrequencies of electrons and ions, respectively, and ν_{ea} and ν_{ia} are the electron–atom and the ion–atom collision frequencies, respectively. Electrons, then, are magnetized and ions are dragged by the neutral plasma component, which gives rise to a radial electric charge-separating field E_r [14]. The field E_r along with the original magnetic field B_z generate the Hall current j_φ that strengthens B_z [20]. The magnetic field is strengthened until the 'raking' of the background magnetic field is compensated by the magnetic field diffusion due to anisotropic plasma conductivity. As a result, a stationary magnetic flux tube is formed in which the magnetic field is determined by the total energy deposition of the convective plasma flux over the tube formation time (around R_0/V_r, where $R_0 \sim 30{,}000$ km is the supergranulation cell scale, and $V_r \sim 0.1 - 0.5$ km s^{-1} is the horizontal velocity of the convective motion). The magnetic field energy density inside the tube can strongly exceed the density of the kinetic energy of the convective motion. In a steady state, the radial gradient of the magnetic field inside the tube is balanced by the gas-kinetic pressure gradient, and the kinetic energy of the convective flux is spent to sustain the field E_r and the Hall current j_φ.

Region 2 is located in the lower photosphere or immediately under it. In this region, the electric current I flowing through the magnetic loop is closed. The electric current distribution in the photosphere, found from magnetic field measurements [21], indicates the presence of noncompensated electric currents [17], i.e., the electric current in the magnetic tube flows through the coronal part of the loop from one footpoint to another. No signatures of the back current have been found. The current is closed in the subphotospheric region (the level $\tau_{5000} = 1$), where the plasma conductivity is isotropic and the current flows along the shortest route from one loop's footpoint to another. Calculations [20] show that at $V_r = 0.1$ km s^{-1} the radius of the tube formed at a height of 500 km above the level $\tau_{5000} = 1$ is $r \approx 3.3 \times 10^7$ cm, and the current is $I \approx 3 \times 10^{11}$ A for the magnetic field $B = 1000$ G at the loop axis.

Region 3 is the coronal part of the loop. Here, the gas-kinetic pressure is below that of the magnetic field (the plasma parameter $\beta \ll 1$) and the loop structure is force-free, i.e., the electric field lines are parallel to the magnetic field lines.

The generalized Ohm law

$$\mathbf{E}^* = \frac{\mathbf{j}}{\sigma_0} + \frac{\mathbf{j}\times\mathbf{B}}{enc} - \frac{\nabla p_e}{en} + \frac{F}{cnm_i\nu_{ia}}\left[(n_a m_a \mathbf{g} - \nabla p_a)\times\mathbf{B}\right] - \frac{F^2}{cnm_i\nu_{ia}}\,\rho\,\frac{\mathrm{d}\mathbf{V}}{\mathrm{d}t}\times\mathbf{B}\,, \tag{1}$$

along with the Maxwell equations, the equation of plasma motion as a whole:

$$\rho\,\frac{\mathrm{d}\mathbf{V}}{\mathrm{d}t} = \rho\mathbf{g} - \nabla p + \frac{1}{c}\,\mathbf{j}\times\mathbf{B}\,, \tag{2}$$

and the continuity equation

$$\frac{\partial\rho}{\partial t} + \mathrm{div}\,(\rho\mathbf{V}) = 0 \tag{3}$$

self-consistently describes the behavior of the plasma and electromagnetic fields in the flare arch with electric current [13, 18, 20]. Here, F is the relative density of the neutrals, and $\mathbf{E}^* = \mathbf{E} + \mathbf{V}\times\mathbf{B}/c$. The remaining notions are well known.

The Joule dissipation of the current, $q = \mathbf{E}^*\mathbf{j}$, taking into account formulas (1)–(3) is represented in the form [13]

$$q = \frac{j^2}{\sigma_0} + \frac{F^2}{c^2 nm_i\nu_{ia}}\,(\mathbf{j}\times\mathbf{B})^2\,. \tag{4}$$

It can be seen that in the force-free ($\mathbf{j}\parallel\mathbf{B}$) field the second term is insignificant and the current dissipation is determined by the Spitzer conductivity σ_0. The dissipation is most effective at $\mathbf{j}\perp\mathbf{B}$. The reason for the enhanced current dissipation (the Cowling resistance) in the coronal arch can be the balloon mode of flute instability of the chromosphere or the protuberance above the arch (see Fig. 1). The 'tongue' of partially ionized plasma penetrating into the current channel deforms the magnetic field, thus providing nonstationarity and injection of neutrals into the current channel. As a result, an Ampere force appears that provides enhanced current dissipation. By integrating formula (4) over the arch's volume, we find the power of energy release:

$$\frac{dW}{dt} = \left[\frac{m_e(\nu_{ei} + \nu_{ea})d}{e^2 nS} + \frac{2\pi F^2 I^2 d}{c^4 n m_i \nu_{ia} S^2}\right] I^2 = \left[R_c + R_{nl}(I)\right] I^2 , \quad (5)$$

where S is the cross section of the arch, and d is the size of the flute 'tongue'. The effect of significant Joule dissipation increase in partially ionized gas was first noted by Schluter and Biermann [22]. This effect is due to large energy loss by ions moving through a gas of neutral particles under the action of the Ampere force $\mathbf{j} \times \mathbf{B}$. Estimates [13, 18] suggest that for the current $I \approx 3 \times 10^{11}$ A, the Cowling resistance in the chromosphere is $R_{nl} \approx 10^{-2}\ \Omega$, and in the corona $R_{nl} \approx 10^{-3} - 10^{-4}\ \Omega$, which provides the observed flare power of about $10^{19} - 10^{21}$ W. Note that the 'anomalous' resistance due to the Buneman or ion–sound instabilities can exceed the Cowling resistance only when the current in the arch is filamented with the cross-section area of the current filaments $S_{fil} \approx 10^9 - 10^{11}\ \text{cm}^2 \ll S \approx 10^{16} - 10^{18}\ \text{cm}^2$.

2.2 The flare arch as an equivalent *RLC* circuit

By excluding velocity variations from equations (1) and (2) and expressing electric field through electric current variations and then integrating over the magnetic loop volume, we obtain the equation for low-amplitude current oscillations $|I_\sim| \ll I$ [23]:

$$\frac{1}{c^2} L \frac{\partial^2 I_\sim}{\partial t^2} + R(I) \frac{\partial I_\sim}{\partial t} + \frac{1}{C(I)} I_\sim = 0 . \quad (6)$$

Here, the following notation was used:

$$R \approx 4 \frac{I^2 l F^2}{c^4 n m_i \nu_{ia} \pi r^4} , \quad C \approx \frac{c^4 n m_i S^2}{2\pi l I^2} , \quad L \approx 4l\left(\ln \frac{8l}{\pi r} - \frac{7}{4}\right) , \quad (7)$$

where l is the major radius of a loop. From relationships (7) it follows that the flare arch has the proper oscillation period which for a sufficiently large current is inversely proportional to its value [23]:

$$P = \frac{2\pi}{c} \sqrt{LC(I)} \approx 10 \frac{S_{17}}{I_{11}}\ [\text{s}] , \quad (8)$$

where $S_{17} = S/10^{17}$ [cm^2], and $I_{11} = I/10^{11}$ [A]. These oscillations are distinguished by a high quality factor

$$Q_{RLC} = \frac{1}{cR} \sqrt{\frac{C}{L}} \sim 10^2 - 10^4 . \quad (9)$$

The proper *RLC*-oscillations of the magnetic arch modulate its radiation intensity of both a thermal and nonthermal nature. Using formula (8), one can determine the electric current amplitudes from pulsation periods of solar flare radiation. Table 1 lists the date and time (UT) of millimeter wave bursts with pulsations, which were observed over a period 1989–1993 by the Metsähovi solar radio telescope (Finland), and their characteristics for typical sizes of flare arches in the Sun [23]. A spectral analysis revealed the radiation modulation with periods from 0.7 to 17 s, which gives the electric current $I \approx 6 \times 10^{10} - 1.4 \times 10^{12}$ A. The total energy of the electric current, stored in the circuit, amounts to $LI^2/2 \approx 10^{30} - 5 \times 10^{32}$ erg.

Table 1. Characteristics of millimeter wave solar radiation bursts with high-quality pulsations (Metsähovi) and parameters of the equivalent *RLC* circuit.

Date	Time of the burst (UT)	Flux, s.f.u.*	P, s	I, 10^{11} A	$LI^2/2$, 10^{31} erg	Flare energy, 10^{29} erg
22.06.89	14:47–14:59	< 150	5.2	2.0	1.0	1.0–4.5
19.05.90	13:15–13:40	10	0.7	14.2	50.0	—
01.09.90	7:06–7:30	27	1.1	9.1	20.9	—
24.03.91	14:11–14:17	< 700	10.0	1.0	0.25	—
07.05.91	10:36–11:00	18	8.3	1.2	0.36	1.3–1.8
16.02.92	12:36–13:20	≈ 2000	5.0	2.0	1.0	—
08.07.92	9:48–10:10	≈ 2500	3.3	3.0	2.3	—
08.07.92	10:15–11:00	15	16.7	0.6	0.08	—
27.06.93	11:22–12:00	40	3.5	2.8	2.0	—

* s.f.u. – solar flux unit.

The stored energy was compared with the flare energy for two events (22.06.89 and 07.05.91). In these flares, $\leqslant 5\%$ of the energy stored in the flare arch was released. Such a situation is realized when the magnetic structure is not destroyed after the flare.

As the solar flare is accompanied by current dissipation, the frequency of *RLC*-oscillations must decrease during the flare. In contrast, if the current builds up in the arch as a result of the photospheric emf action, the frequency of *RLC*-oscillations will increase. The search for signals with linear frequency modulation (LFM) (whose frequency is $\omega = \omega_0 + Kt$, where K is a constant) with positive and negative frequency drifts in the low-frequency (LF) modulation spectrum of flare emission, observed at a frequency of 37 GHz by the Metsähovi radio telescope, was carried out in Ref. [24] using the Wigner–Ville transform [25]. An example of such an analysis is shown in Fig. 2.

In the event on 24.03.91, the current in the loop decreased from 9×10^{11} A at the beginning of the burst to 10^{11} A at the final stage. The power released was 10^{21} W. After the flare (14:50 UT), the drift velocity of the LFM signal became positive, indicating that the energy accumulation starts again. This example can be considered as experimental evidence for

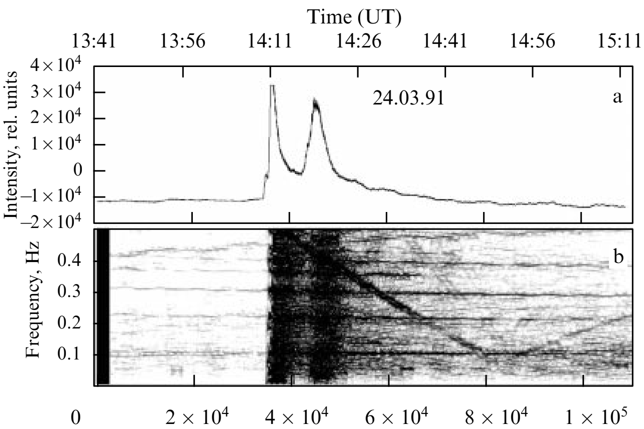

Figure 2. Burst of solar flare emission on 24.03.1991 (14:05 UT) from active region S25W03 at a frequency of 37 GHz and the dynamical spectrum of its pulsations [24].

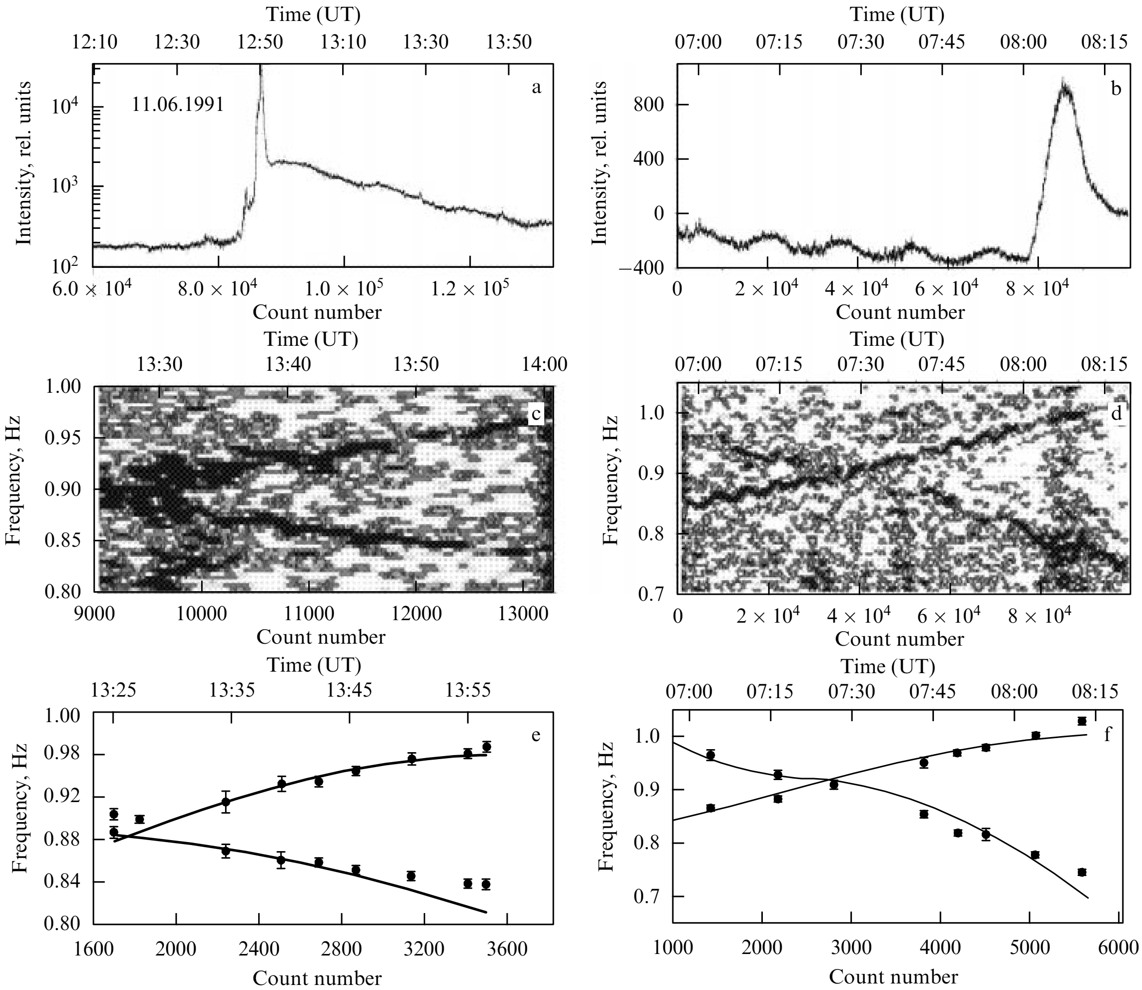

Figure 3. Emission time profiles of solar flares dated 11.05.1991 (a) and 13.07.1992 (b) at the frequency 37 GHz (Metsähovi); (c, d) dynamical spectra of the LF-modulation of the emission as obtained by the Wigner – Ville method; (e, f) results of modeling these dynamical spectra by *RLC*-oscillations of two inductively interacting magnetic arches [26].

the dissipation and storage of energy of electric current in coronal arches.

2.3 Inductive interaction of two current-carrying arches

Equation (6) is valid for a loop magnetically isolated from surrounding loops, i.e., it ignores the mutual induction effect due to the external magnetic flux changing through the loop contour. This effect can be included into integration of the generalized Ohm law by adding to the quantity

$$\int \frac{\partial E_z}{\partial t}\, \mathrm{d}l = -\frac{L}{c^2}\frac{\partial^2 I}{\partial t^2}$$

the electromotive force of the mutual induction, viz.

$$\frac{1}{c^2}\frac{\partial^2}{\partial t^2}\left[\sum_j^N M_j I_j\right],$$

where I_j is the current in the jth loop, M_j is the mutual induction coefficient between the jth loop and the considered one, and the summation is performed over loops surrounding the preferred one. The influence of the surrounding loops can be ignored when studying relatively rapid *RLC*-oscillations of the electric current in the loop. Slow current variations due to induction interaction with surrounding loops will lead to the *RLC*-frequency drift, which must be manifested in the LF spectra. The reason for slow current variations can be the induction emf that appears during interaction of a magnetic loop with other loops in the course of their rising or relative motion. Equations for slow current variations in two induction-interacting magnetic loops are written down in the following form [26] :

$$\frac{1}{c^2}\frac{\partial}{\partial t}(L_1 I_1 + M_{12} I_2) + I_1 R_1(I_1) = \Xi_1\,,$$
$$\frac{1}{c^2}\frac{\partial}{\partial t}(L_2 I_2 + M_{21} I_1) + I_2 R_2(I_2) = \Xi_2\,. \tag{10}$$

Here, $L_{1,2}$ and $R_{1,2}(I_{1,2})$ are the inductances and resistances of the loops, respectively, defined by formulas (7), and $\Xi_{1,2}$ are electromotive forces in the photospheric footpoints of the loops. The mutual induction coefficients can be approximated by the formula

$$M_{12} = M_{21} = 8(L_1 L_2)^{1/2}\,\frac{R^{(1)}_{\mathrm{loop}} R^{(2)}_{\mathrm{loop}}}{(R^{(1)}_{\mathrm{loop}} + R^{(2)}_{\mathrm{loop}})^2 + d^2_{1,2}}\cos\varphi\,, \tag{11}$$

where $R^{(1,2)}_{\mathrm{loop}}$ are the major radii of the loops, $d_{1,2}$ are the distances between the centers of the toroids, and φ is the angle

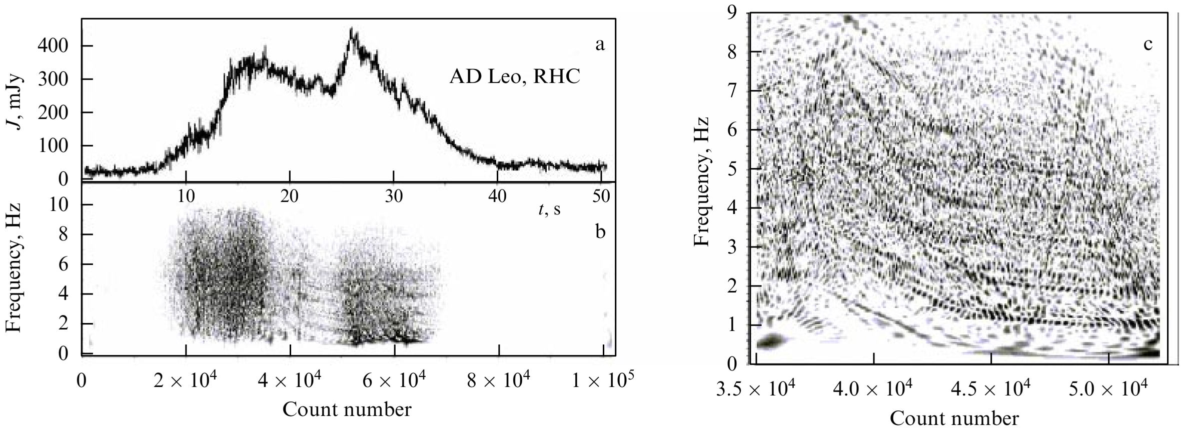

Figure 4. (a) Light curve of a flare from AD Leo on May 19, 1997 at the frequency 4.85 GHz, obtained on the right-hand circular (RHC) polarization of waves. J is the radiation flux (the maximum value reaches 400 mJy), and the flare duration is 50 s. (b) The spectrum of pulsations obtained by the Wigner – Ville method. (c) A zoomed fragment of the spectrum [27].

between normals to the toroid planes. Equations (10), (11) were used in Ref. [26] to model binary tracks that appear in the low-frequency modulation spectra of the flare microwave radiation intensity (Fig. 3).

2.4 Pulsating radio bursts from AD Leo star

Solar – stellar analogs are successfully applied to explain stellar activity. This can be exemplified by an analysis of radio emission from the active red dwarf AD Leo. Observations revealed quasiperiodic pulsations with periods from 1 to 10 s. Phenomenologically, the stellar pulsations are similar to pulsations of type IV solar radio emission, but there are also some differences.

A dynamical spectrum of radio pulsations from an AD Leo flare registered on May 19, 1997 (18.57 UT) by the Effelsberg 100-m radio telescope was calculated in Ref. [27] (Fig. 4). The time profile (Fig. 4a) illustrates fluctuations of radio radiant flux, which have a pulsational character in the dynamical spectrum of the burst (Fig. 4b).

Figure 4c depicts a fragment of the pulsation spectrum in the 0 – 9-Hz range, obtained by the Wigner – Ville transform for the decaying part of the first emission pulse. The spectrum suggests two independent types of modulation simultaneously acting on the radio source: (1) periodic short pulses with the pulse repetition rate $\nu_1 = 2$ Hz, and (2) a sine wave with the frequency $\nu_2 = 0.5$ Hz. A preliminary analysis of pulsations from AD Leo [28] demonstrated that the source of the radio flare on May 19, 1997 was a coronal magnetic arch with the particle number density $n \approx 2.3 \times 10^{11}$ cm^{-3}, temperature $T = 3 \times 10^7$ K, and magnetic induction $B = 730 - 810$ G. Based on these data, it can be concluded that the pulse modulation is due to fast magnetoacoustic oscillations of the magnetic loop with the frequency $\nu_1 \approx V_A/r$, where $V_A = B/\sqrt{4\pi m_i n}$ is the Alfvén velocity, and r is loop's radius. Assuming $\nu_1 = 2$ Hz, the Alfvén velocity is estimated to be $V_A \approx 3.5 \times 10^8$ cm s^{-1}, and $r \approx 1.8 \times 10^8$ cm, which is comparable to the radius of flare magnetic arches in the Sun.

The sinelike modulation (see Fig. 4) is most likely attributed to oscillations of the magnetic arch as an equivalent *RLC* circuit with period (8). The negative frequency drift of the modulating signal is explained by the dissipation of the electric current during the flare. Using $\nu_2 = 0.5$ Hz and peculiarities of the LFM-signal spectrum, we can evaluate the flare arch length of AD Leo to be $l \approx 4 \times 10^{10}$ cm, which is on the order of the radius of the star, the value of the electric current $I \approx 4.5 \times 10^{12}$ A, the energy $W \approx LI^2/2 \approx 5.5 \times 10^{26}$ J of the electric current stored in the flare, and the energy release rate $\dot{W} \approx 10^{25}$ W [27]. The last quantity is 3 – 4 orders of magnitude higher than that in a solar flare. This is due to large magnetic fields on the red dwarf surface and an enhanced photospheric convection.

3. Acceleration of charged particles and their propagation features

3.1 Charged particle acceleration in the flare

A substantial fraction of flare energy is released in the form of energetic particles. In this case, electrons and ions are accelerated up to energies 100 keV and 100 MeV, respectively [29], thus producing hard X-ray and gamma radiation. According to a nonthermal model, an impulsive solar flare produces 10^{37} electrons per second with energies above 20 keVfor 100 s. This means that the energy release rate in the form of accelerated electrons equals 3×10^{29} erg s^{-1}, which corresponds to a total electron energy $E_e\,(>20$ keV$) \approx 3 \times 10^{31}$ erg for a total number of accelerated electrons equal to $N_e\,(>20$ keV$) \approx 10^{39}$. Requirements for the acceleration rate are less stringent in the hybrid model [30] which assumes an X-ray emission spectrum below 30 keV as originating from the radiation of hot ($T \sim 3 \times 10^7$ K) plasma; at higher energies, radiation is generated by fast electrons. In that case, the required production rate of electrons with energies above 20 keV reduces to 2×10^{35} electrons per second. For an acceleration process duration of 100 s this yields $N_e\,(>20$ keV$) \approx 2 \times 10^{37}$ and $E_e\,(>20$ keV$) \approx 6 \times 10^{29}$ erg. Therefore, to provide the observed flux of fast electrons, a sufficiently large number of particles ($\geqslant 2 \times 10^{37}$) must be being accelerated. What is the particle reservoir if the acceleration occurs in a flare arch? The number of particles in the arch having plasma density 10^{10} cm^{-3}, cross-section area 10^{18} cm^2, and length $(1-5) \times 10^9$ cm ranges $(1-5) \times 10^{37}$. Any conceivable mechanism accelerates only an insignificant fraction of particles, so that the number of accelerated electrons in the coronal arch proves to be insufficient for providing acceleration even in the favorable case of the hybrid model ($\sim 2 \times 10^{37}$ electrons). In this connection, *the problem of involving a sufficient number of charged particles into the acceleration process emerges.*

In a magnetic arch, two potential sources can supply the required number of particles. The first source is related to the chromospheric part of the arch, where there are $\sim 5 \times 10^{40}$ particles in the column with a length extending from the minimum temperature layer to the transition region, if one assumes the loop's cross-section area to be of about 10^{18} cm^2. The second possibility of enriching the flare loop with charged particles emerges during its interaction with dense matter of the prominence, which yields $\approx 3 \times 10^{38}$ particles [13]. This implies that in order to supply the acceleration mechanism with particles during energetic flares, the chromospheric part of the coronal arch should be the preferential location for the acceleration region. For moderate flares, the acceleration region can lie near the top of the arch.

To explain the generation of fast particles in flares, different acceleration mechanisms have been invoked: stochastic acceleration by waves, acceleration by shocks, betatron acceleration, and acceleration in quasistationary (DC) electric fields. The most effective acceleration is provided by the large-scale electric field $\mathbf{E}$ of the flare magnetic loop. If a magnetic field $|\mathbf{B}| > |\mathbf{E}|$ is present in the plasma, particles will be accelerated only by the projection of the electric field onto the magnetic one, $E_{\parallel} = \mathbf{EB}/B$. If the value of $E_{\parallel}$ is below the Dreicer field $E_{\mathrm{D}} = e\Lambda\omega_{\mathrm{p}}^2/V_T^2$, then electrons with the velocities $V > (E_{\mathrm{D}}/E_{\parallel})^{1/2} V_T$ (where V_T is the thermal electron velocity, Λ is the Coulomb logarithm, and ω_{p} is the Langmuir frequency) start accelerating (and are known as runaway electrons). The production rate of runaway electrons is given by [31]

$$\dot{N}_{\mathrm{e}} = 0.35\, n\nu_{\mathrm{ei}} V_{\mathrm{a}} x^{3/8} \exp\left(-\sqrt{2x} - \frac{x}{4}\right), \tag{12}$$

where $x = E_{\mathrm{D}}/E_{\parallel}$, and V_{a} is the acceleration region volume. The strongest electric fields are generated at the magnetic loop footpoints where an effective charge separation emerges due to the convective flux of the photospheric matter into the tube and a different degree of magnetization of electrons and ions. The expression for $E_{\parallel}$ was derived in Ref. [32]:

$$E_{\parallel} \approx \frac{1-F}{2-F} \frac{\sigma_0 V_r B^2}{enc^2(1+\mu B^2)} \frac{B_r}{B}. \tag{13}$$

Here, the radial component of the magnetic field is $B_r \ll B$, and $\mu = \sigma_0 F^2/(2-F)c^2 n m_{\mathrm{i}} \nu_{\mathrm{ia}}$. The particle acceleration due to the charge-separating field can occur when flute instability is set in at the loop footpoints, when the plasma 'tongue' invading the current channel is inhomogeneous in height. The accelerating field at $B_r \approx 0.1B$ can attain the value of the Dreicer field and even exceed it [32]. All electrons then undergo runaway, and the electric field becomes as high as 17 V cm^{-1}. This makes it possible for particles to acquire a maximum possible energy of $\sim$ 1 GeV on the scale of length of about 10^8 cm. The extremal electric fields are set in for magnetic fields $\sim 10^3$ G and under strong heating of the photospheric footpoints of the magnetic arch, which does not occur in all flares. However, this demonstrates possibilities of the current-carrying magnetic arches to efficiently accelerate particles. For acceleration at the chromospheric footpoints of the arch, the production rate of energetic electrons will exceed 10^{35} electrons per second, which is sufficient for the hybrid model on the assumption of $n = 10^{11}$ cm^{-3} inside the acceleration region, the tube radius 10^8 cm, $T = 10^5$ K, and the acceleration region height $h = 10^8$ cm. Then, $x = E_{\mathrm{D}}/E_{\parallel} = 26$, $E_{\parallel} \approx 2 \times 10^{-3}$ V cm^{-1}, and the energy of the greater part of accelerated electrons will reach 200 keV.

A good illustration of the charged particle acceleration in quasistationary electric fields, when electrons and ions are accelerated in opposite directions, is provided by the flare of July 23, 2002. According to the RHESSI data [33], the X-ray emission in the range from 150 to 200 keV, generated by fast electrons, emanates from one footpoint of the flare arch, while gamma-ray emission line 2.223 MeV generated by fast ions originates from another one.

As the acceleration mechanism produces $\geqslant 10^{35}$ electrons per second, the electric current $I \geqslant 10^{15}$ A is set in. By flowing along the magnetic arch with cross-section area $\sim 10^{18}$ cm^2, this current must induce a magnetic field $B \geqslant 6 \times 10^6$ G, which is not observed in coronal arches (*the Colgate paradox*). Two possibilities of resolving this paradox have been discussed. The first possibility assumes that the current channel can be split into many current filaments with currents flowing in opposite directions in the neighboring filaments, which results in a total magnetic field below the observed value [34]. It is unclear, however, how filaments with opposite directions of currents can emerge in the accelerated electron beam. Another possibility is related to the formation of reverse current in plasma [35]. Let an electron beam be injected into a plasma along the external magnetic field B_z. Then the field B_{φ} at any given point in the plasma will change with time as the leading edge of the flux propagates. Changing B_{φ} gives rise to an electric field E_z appearing at the leading edge of the propagating electron beam. This field acts on plasma electrons in such a way that a current opposite to the injected one appears. Hence, the total current is reduced until complete compensation. According to the Lentz rule, the beam of accelerated electrons can propagate in plasma without expending energy to modify the magnetic field.

3.2 Turbulent regime of propagation of energetic particles

The wave – particle interaction in the solar corona manifests itself in the peculiar character of propagation of energetic particles. For example, in the flare of August 28, 1999 [36], relativistic electrons generating synchrotron radiation at the frequency 17 GHz moved along a coronal magnetic arch with a velocity 30 times less than the speed of light (Fig. 5). This phenomenon can be explained in terms of strong turbulent diffusion [37, 38]. A low-frequency whistler turbulence excited by the electron flux effectively scatters relativistic particles through the pitch angle. As a result, instead of freely propagating, the electrons, due to the anomalous (turbulent) viscosity, move with a velocity on the order of the phase velocity of whistlers, namely $\approx 0.03c$ (line A). At the next injection (line B), whistles did not affect the particle propagation.

The absence of noticeable ($< 0.07\%$) linear polarization of the H_{α}-emission generated by energetic proton beams decelerating in the chromosphere [30] provides the second example. The most likely reason for this occurring is the scattering of the radiation on small-scale Alfvén waves excited at the ion cyclotron resonance by protons with energies $\sim$ 1 MeV, which leads to radiation isotropy. Here, protons are effectively scattered through pitch angles (strong diffusion) if the power of the energy particle accelerator

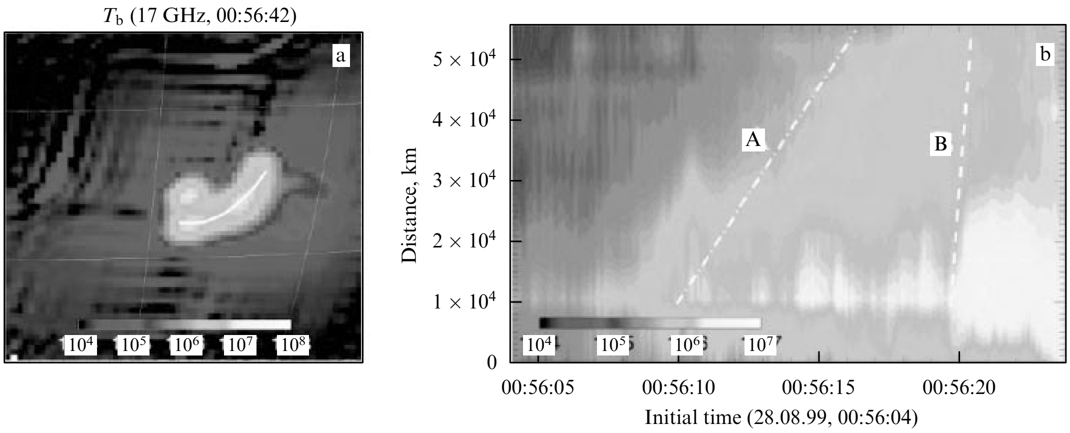

Figure 5. (a) The image of the flare dated 28.08.1999, consisting of two sources and obtained by the Nobeyama radioheliograph at the frequency 17 GHz at 00:56:42 UT. The light line in the center of the figure shows the trajectory of relativistic electrons propagating in an extended arch 5×10^4 km in length [36]. T_b is the brightness temperature of the microwave radiation, $10^4 < T_b < 10^8$ K. The lighter regions correspond to higher temperatures. (b) The propagation of the microwave signal with the velocity $v = 0.03c$ at the first stage of acceleration of energetic electrons (line A), and with the velocity $v \sim c$ at the second acceleration stage (line B).

exceeds $J_* = 5 \times 10^{12}$ protons per cm^2 per s. The data on energetic particles in solar flares suggest an acceleration rate of protons with energies above 1 MeV on the order of $10^{33}-10^{34}$ protons per s [29]. Assuming the area of the proton invasion region into the chromosphere to be $\sim 10^{18}$ cm^2, we find the flux $J \sim (10^{15}-10^{16})$ cm^{-2} s$^{-1} \gg J_*$. The strong diffusion regime also leads to a time delay of the gamma-ray line emission relative to hard X-ray emission from flares [40], since the velocity of the turbulent front created by ions is an order of magnitude below that of the turbulent 'wall' formed by fast electrons.

4. Eigen-mode oscillations of loops and flare plasma diagnostics

The TRACE satellite observations of the Sun discovered oscillations of the coronal arches above active regions [41], which stimulated the development of a promising field in astrophysics — coronal seismology. These studies were initiated by Dutch physicist H Rosenberg [42] who related pulsations of type IV solar radio emission to magnetohydrodynamic (MHD) oscillations of the coronal arch. At the boundary between the arch and the external medium there is an impedance jump for MHD waves, so that the coronal arch can be considered a resonator. Pulsating emission over different wavebands (optical, X-ray, radio) is observed not only from the Sun, but also from flare stars. Interest in oscillations of arches is related to feasibility of explaining coronal heating mechanisms and upgrading flare diagnostic techniques.

Coronal arch oscillations are studied by modeling a plasma cylinder with radius r and length l with ends 'frozen' into a superconducting medium. Plasma parameters inside and outside the cylinder are the following: density ρ_i, temperature T_i, and magnetic field B_i, as well as ρ_e, T_e, and B_e, respectively. The dispersion equation relating the cylinder oscillation frequency ω to the wave vector components $k_\perp$ and $k_\parallel$ has the form [43, 44]

$$\frac{J'_m(\varkappa_i r)}{J_m(\varkappa_i r)} = \alpha \, \frac{H_m^{(1)'}(\varkappa_e r)}{H_m^{(1)}(\varkappa_e r)}\,, \tag{14}$$

where

$$\varkappa^2 = \frac{\omega^4}{\omega^2(C_S^2 + V_A^2) - k_\parallel^2 C_S^2 V_A^2} - k_\parallel^2\,,$$

$$\alpha = \frac{\varkappa_i \rho_i}{\varkappa_e \rho_e}\,\frac{\omega^2 - k_\parallel^2 V_{Ai}^2}{\omega^2 - k_\parallel^2 V_{Ae}}\,,$$

C_S is the speed of sound, J_m and $H_m^{(1)}$ are the Bessel and Hankel functions of the first kind, respectively, $k_\parallel = \pi s/l$, and $s = 1, 2, 3, \ldots$. For a thin $(r/l \ll 1)$ and dense $(\rho_e/\rho_i \ll 1)$ cylinder at $m = 0$, from formula (14) it follows that the frequency of fast magnetosonic (sausage) oscillations, which mostly modulate emission from arches, is given by

$$\omega_+ = (k_\perp^2 + k_\parallel^2)^{1/2}(C_{Si}^2 + V_{Ai}^2)^{1/2}\,. \tag{15}$$

The transverse wave number is $k_\perp = \lambda_i/r$, where λ_i are zeros of the Bessel function, and $J_0(\lambda) = 0$. Estimates [45] show that the electron plasma heat conductivity is the most important reason for sausage oscillation decay in solar arches. Therefore, their quality factor is defined as

$$Q = \frac{\omega_+}{\gamma} \approx \frac{2m_e}{m_i}\,\frac{P\nu_{ei}}{\beta^2 \sin^2 2\theta}\,, \tag{16}$$

where $\theta = \arctan(k_\perp/k_\parallel)$, $P = 2\pi/\omega_+$ is the period of oscillations, and γ is the wave decay decrement. In the course of sausage oscillations, modulation of the flux of gyrosynchrotron emission of energetic electrons with a power-law energy spectrum with index δ for an optically thin source has the form [45]

$$\varDelta = 2\xi\,\frac{\delta B}{B} = \xi\beta\,, \qquad \xi = 0.9\delta - 1.22\,. \tag{17}$$

Taking into account the curvature of magnetic field and a sufficiently large parameter β, the balloon mode of flute instability can be excited in coronal arches. The ballooning oscillations result from the joint action of the destabilizing force $F_1 \sim p/R_{loop}$ related to the pressure gradient and the

Table 2. Formulas to determine parameters of a flare from emission pulsations caused by ballooning and sausage oscillations of a magnetic arch. Here, $\chi = 10\varepsilon/3 + 2$, $\tilde{r} = 2.62r$, $\varepsilon = \Delta/\xi$, temperature T is expressed in K, particle number density n is in cm^{-3}, and magnetic field B is in G.

Ballooning oscillations	Sausage oscillations
$T = 2.42 \times 10^{-8}\,\dfrac{l^2\varepsilon_1}{N^2P_1^2}$	$T = 1.2 \times 10^{-8}\,\dfrac{\tilde{r}^2\varepsilon}{P^2\chi}$
$n = 5.76 \times 10^{-11}\,\dfrac{Q_1 l^3\varepsilon_1^{7/2}}{N^3P_1^4}\sin^2 2\theta$	$n = 2 \times 10^{-11}\,\dfrac{Q\tilde{r}^3\varepsilon^{7/2}}{P^4\chi^{3/2}}\sin^2 2\theta$
$B = 6.79\times 10^{-17}\,\dfrac{Q_1^{1/2} l^{5/2}\varepsilon_1^{7/4}}{N^{5/2}P_1^3}\sin 2\theta$	$B = 2.9\times 10^{-17}\,\dfrac{Q^{1/2}\,\tilde{r}^{5/2}\varepsilon^{7/4}}{P^3\chi^{5/4}}\sin 2\theta$

curvature of magnetic field and the restoring force $F_2 \sim B^2/R_{\text{loop}}$ arising from the tension of the magnetic field lines. The period of oscillations equals

$$P_1 = \frac{2l}{V_{\text{A}}}\left(N^2 - \frac{l\beta}{2\pi d}\right)^{-1/2} \approx \frac{2l}{V_{\text{A}}N}\,, \qquad (18)$$

where N is the number of oscillating regions present along the loop's length l. Estimates indicate that the ballooning oscillations in the atmosphere of the Sun also decay because of electron plasma heat conductivity. Equations for the frequency of oscillations (15), (18), the quality factor (16), and the emission modulation depth (17) can be used for determining the temperature and density of plasma and the magnetic field in the arch (Table 2).

Two examples of applying such diagnostic techniques are given in Ref. [45]. Observations of the solar flare of May 8, 1998 (01:49 – 02:17 UT) in the form of a single arch at the frequency 17 GHz (the Nobeyama radioheliograph) and in the hard X-ray range (the Yohkoh satellite) testify to the presence of ballooning oscillations with the parameters $l = 8 \times 10^9$ cm, $N = 4$, $\theta = 66°$, $\Delta_1 \approx 0.3$, $Q_1 \approx 25$, and $\delta = 3.5$. Using formulas from Table 2, we find $T \approx 5.9 \times 10^7$ K, $n \approx 1.4 \times 10^{11}$ cm^{-3}, $B \approx 425$ G, and the plasma parameter $\beta \approx 0.16$.

The solar flare of August 28, 1999 (00:55 – 00:58 UT) illustrates the interaction of two arches: a compact one and an extended one (see Fig. 5). A wavelet analysis revealed the characteristic pulsation periods 14 and 2.4 s. The scenario of the event is as follows. The flaring energy release was accompanied by exciting ballooning oscillations with $P_1 = 14$ s in a compact source. The gas pressure increase led to the development of an aperiodic mode of ballooning instability and the interaction of the compact source with the neighboring arch (loop – loop interaction), which was accompanied by an injection of hot plasma and energetic particles. Because oscillations with the period $P = 2.4$ s were set up after the plasma injection, they are most likely due to sausage modes of the extended source. Applying the formulas from Table 2, the analysis of the pulsations yields the following parameters of the compact and extended arches:

$$T \approx 4.6 \times 10^7 \text{ K}, \quad n \approx 10^{11} \text{ cm}^{-3}, \quad B \approx 300 \text{ G}, \quad \beta \approx 0.18\,;$$

$$T \approx 2.1 \times 10^7 \text{ K}, \quad n \approx 10^{10} \text{ cm}^{-3}, \quad B \approx 120 \text{ G}, \quad \beta \approx 0.06\,,$$

respectively. The compact arch is linked to the primary source of energy release and demonstrates higher values of temperature, density and the magnetic field.

5. Conclusion

We have shown that coronal magnetic loops (arches) play an important role in the origin of solar flare activity. Strong electric currents that initiate an explosive energy release, when flute instability develops, can flow in the arches. Flute instability (the ballooning mode) can be responsible both for charged particle acceleration and plasma injection into the neighboring arch via loop – loop interaction.

The mechanism of acceleration in quasistationary electric fields is crucial for particle acceleration in flares. The wave – particle interaction effect determines the dynamics of energetic particles in the solar atmosphere.

The approximation of a current-carrying arch in the form of an equivalent electric circuit and resonator for MHD waves reflects the physics of processes in flares. The flare arch possesses a set of proper frequencies that result in a low-frequency modulation of the emission in a wide wavelength range (optical, radio, X-ray). The rapidly evolving field of modern astrophysics — coronal seismology — based on these approaches provides a powerful diagnostic technique for flare plasma.

This work is supported by the Program 'Solar Activity' of the Presidium of RAS, by the Program OFN-16, and by the RFBR grants 06-02-16859, 04-02-39029GFEN, and 05-02-16252.

References

1. Sweet P A, in *Electromagnetic Phenomena in Cosmical Plasma* (Intern. Astron. Union Symp., No. 6, Ed. B Lehnert) (Cambridge: Univ. Press, 1958) p. 123
2. Gold T, Hoyle F *Mon. Not. R. Astron. Soc.* **120** 89 (1960)
3. Sturrock P A *Astron. J.* (Suppl.) **73** 78 (1968)
4. Heyvaerts J, Priest E R, Rust D M *Astrophys. J.* **216** 123 (1977)
5. Parker E N *Astrophys. J.* **180** 247 (1973)
6. Spicer D S *Solar Phys.* **53** 305 (1977)
7. Sakai J-I, de Jager C *Space Sci. Rev.* **77** 1 (1996)
8. Syrovatskii S I *Astron. Zh.* **43** 340 (1966) [*Sov. Astron.* **10** 270 (1966)]
9. Somov B V *Physical Processes in Solar Flares* (Dordrecht: Kluwer Acad. Publ., 1992)
10. Alfvén H, Carlqvist P *Solar Phys.* **1** 220 (1967)
11. van Hoven G, in *Solar Flare Magnetohydrodynamics* (Fluid Mechanics of Astrophys. and Geophys., Vol. 1, Ed. E R Priest) (New York: Gordon and Breach Sci. Publ., 1984) Ch. 4
12. Melrose D B, McClymont A N *Solar Phys.* **113** 241 (1987)
13. Zaitsev V V, Stepanov A V *Astron. Zh.* **68** 384 (1991) [*Sov. Astron.* **35** 189 (1991)]; *Solar Phys.* **139** 343 (1992)
14. Sen H K, White M L *Solar Phys.* **23** 146 (1972)
15. Henoux J C, Somov B V *Astron. Astrophys.* **185** 306 (1987)
16. Ionson J A *Astrophys. J.* **254** 318 (1982)
17. Melrose D B *Astrophys. J.* **451** 391 (1995)
18. Zaitsev V V, Urpo S, Stepanov A V *Astron. Astrophys.* **357** 1105 (2000)
19. Klimchuk J A et al. *Publ. Astron. Soc. Jpn.* **44** L181 (1992)
20. Khodachenko M L, Zaitsev V V *Astrophys. Space Sci.* **279** 389 (2002)
21. Leka K D et al. *Astrophys. J.* **411** 370 (1993)
22. Schluter A, Biermann L *Z. Naturforsch. A* **5** 237 (1950)
23. Zaitsev V V et al. *Astron. Zh.* **75** 455 (1998) [*Astron. Rep.* **42** 400 (1998)]
24. Zaitsev V V et al. *Astron. Zh.* **80** 945 (2003) [*Astron. Rep.* **47** 873 (2003)]
25. Cohen L *Proc. IEEE* **77** 941 (1989)
26. Khodachenko M L et al. *Astron. Astrophys.* **433** 691 (2005)
27. Zaitsev V V et al. *Pis'ma Astron. Zh.* **30** 362 (2004) [*Astron. Lett.* **30** 319 (2004)]
28. Stepanov A V et al. *Astron. Astrophys.* **374** 1072 (2001)
29. Miller J A et al. *J. Geophys. Res.* (*Space Phys.*) **102** (A7) 14631 (1997)
30. Holman G D, Benka S G *Astrophys. J.* **400** L79 (1992)

31. Knoepfel H, Spong D A *Nucl. Fusion* **19** 785 (1979)
32. Zaitsev V V, Khodachenko M L *Izv. Vyssh. Uchebn. Zaved. Radiofiz.* **40** 176 (1997)
33. Dennis B R *Lect. Not. Phys.* (2005) (in press)
34. van den Oord G H J *Astron. Astrophys.* **234** 496 (1990)
35. Lee R, Sudan R N *Phys. Fluids* **14** 1213 (1971)
36. Yokoyama T et al. *Astrophys. J.* **576** L87 (2002)
37. Bespalov P A, Trakhtengerts V Yu, in *Voprosy Teorii Plazmy* (Problems in Plasma Theory) Vol. 10 (Ed. M A Leontovich) (Moscow: Atomizdat, 1980) p. 88 [Translated into English: *Reviews of Plasma Physics* Vol. 10 (Ed. M A Leontovich) (New York: Plenum Press, 1986) p. 155]
38. Stepanov A V et al. *Publ. Astron. Soc. Jpn.* (2005) (in press)
39. Bianda M et al. *Astron. Astrophys.* **434** 1183 (2005)
40. Bespalov P A, Zaitsev V V, Stepanov A V *Astrophys. J.* **374** 369 (1991)
41. Aschwanden M J et al. *Astrophys. J.* **520** 880 (1999)
42. Rosenberg H *Astron. Astrophys.* **9** 159 (1970)
43. Zaitsev V V, Stepanov A V, in *Issledovaniya po Geomagnetizmu, Aeronomii, Fizike Solntsa* (Studies in Geomagnetism, Aeronomy and Solar Physics) Issue 37 (Moscow: Nauka, 1975) p. 3
44. Nakariakov V M, Stepanov A V *Lect. Not. Phys.* (2005) (in press)
45. Stepanov A V et al. *Pis'ma Astron. Zh.* **30** 530 (2004) [*Astron. Lett.* **30** 480 (2004)]

PACS numbers: 78.70.Bj, **98.35.–a**, **98.70.–f**
DOI: 10.1070/PU2006v049n03ABEH005969

Annihilation emission from the galactic center: the INTEGRAL observatory results

E M Churazov, R A Sunyaev, S Yu Sazonov, M G Revnivtsev, D A Varshalovich

1. Introduction

The narrow positron annihilation line at the energy 511 keV is the brightest line in the emission spectrum of our Galaxy at energies above 10 keV. A spectral feature at energy ~ 476 keV in the radiation from the galactic center region was discovered more than 30 years ago by detectors with low energy resolution during balloon flights [1]. Soon after, observations carried out with high-resolution Ge detectors reliably identified this feature with the narrow positron annihilation line at 511 keV [2]. Later on, the annihilation emission was detected in several other experiments. Despite repeated observations, no final answer on the nature of the annihilation emission of the Galaxy has been obtained so far. This is primarily due to the existence of several principally different mechanisms for producing positrons, including:

radioactive β^+ decay of unstable isotopes, for example, ^{26}Al or ^{56}Co, produced in supernova and nova explosions;

decay of π^+ mesons arising from the interaction of cosmic rays with matter;

electron – positron pair production in high-energy photon interactions or in strong magnetic fields near compact sources — black holes or radio pulsars, and

production of positrons from dark matter particle annihilation.

Although this list is incomplete, it clearly demonstrates a great diversity of mechanisms discussed — from the commonly accepted (supernova nucleosynthesis) to the most exotic (dark matter annihilation).

Key explanations of the nature of the 511-keV line comprise: (a) determination of the space distribution of the annihilation radiation in the Galaxy and its comparison with that of potential positron sources, and (b) detailed studies of the annihilation radiation spectrum and obtaining restrictions on properties of matter in which the annihilation occurs. These are the problems that should be resolved by the INTEGRAL observatory equipped with a high-resolution Ge spectrometer.

2. Observations and data analysis

The INTEGRAL observatory is a project of the European Space Agency with the participation of Russia and the USA. The observatory was launched into a high-apogee orbit with a period of 3 days by the Proton rocket in October 2002. To investigate the annihilation emission, the SPI device [3] consisting of 19 independent high-purity Ge crystals that provide an energy resolution of about 2 keV at 511 keV was used. A tungsten mask with a thickness of 3 cm was installed at 171 cm from the detector. This mask provides modulation of the radiant flux registered by the detector. The field of view of the telescope is around 30°. In our analysis, we have made use of data obtained in the period from February to November 2003. The total observation time amounted to 3.9×10^6 s [4].

The energy scale in each observation was controlled by the location of bright background lines (^{71} Ge, 198.4 keV; ^{69}Zn, 438.6 keV; ^{69}Ge, 584.5 keV, and ^{69}Ge, 882.5 keV) seen in the spectrum taken by each detector. After such calibration, the typical amplitude of variations with time of the background line locations near 500 keV was less than 0.01 keV. The positron annihilation line is also present in the background spectrum of the SPI telescope. This line is due to positrons produced and annihilated inside detector's body and in the surrounding materials exposed to high-energy charged particles. Because the spectral line produced by the positron annihilation in the telescope material was broadened with respect to telescope intrinsic resolution, the actual energy resolution was determined from interpolation of the observed widths of two lines, 438.6 keV and 584.5 keV, symmetrically located around the 511-keV line. The energy resolution at 511 keV, determined in this way, corresponds to 2.1 keV (full width at half maximum, FWHM) for the entire data set.

Modeling the background spectrum of the telescope has required serious effort. During observations of the Galactic Center region, the background flux at 511 keV is approximately 50 – 100 times above the desired signal, and therefore the background model should predict it with an accuracy much better than 1%. To construct the background model, we have used observed data obtained from different regions of the celestial sphere located at angular distances of more than 30° from the center of the Galaxy. The total exposure of observations used to construct the background model was around 3.7×10^6 s. The model accounts for the background variations related to variations in the charged particle flux and the gradual accumulation of long-lived unstable isotopes inside the detector body.

3. The map of the Galaxy in the 511-keV line

Figure 1 shows the map of the surface brightness of galactic emission in the 511-keV line. In each observation, the detected 508 – 514-keV flux (with the model background

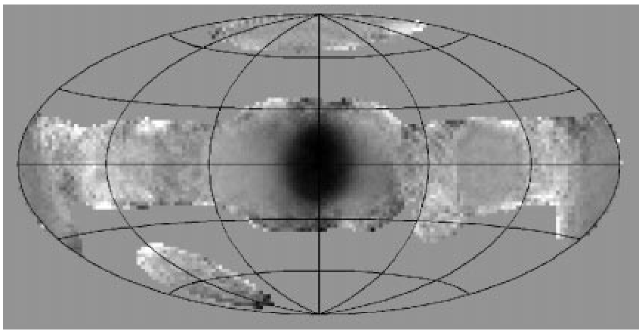

Figure 1. Distribution of galactic surface brightness in the 511-keV line. High surface brightness is shown by dark color. The map is constructed in the galactic coordinates centered at the Galactic Center. The map is strongly smoothed as it is constructed. The central spot shows that the surface brightness of annihilation emission is large in the central zone of the Galaxy, and is small in other directions.

subtracted) was distributed over the section of the celestial sphere within the telescope's field of view with a weight proportional to the effective area for 511-keV photons arriving from the given direction. Thus, the map constructed is the convolution of the true surface brightness distribution of the annihilation emission with a kernel depending on the instrumental field of view and the orientation of the telescope in each observation. On this map, only spatial scales exceeding the size of the field of view are retained, while small-scale structures are strongly suppressed. Nevertheless, this map allows the assessment of the global distribution of the annihilation emission in the Galaxy. In particular, the central region of the Galaxy (the bright spot at the map's center) is apparently a powerful source of the 511-keV line emission. The surface brightness of other regions of the Galaxy is much lower, and intensity variations seen in Fig. 1 correspond to the expected statistical noise.

Stronger restrictions on the surface brightness distribution parameters can be obtained by assuming a model brightness distribution in the Galaxy with several free parameters, and then by convolving this distribution with the instrumental response and comparing the result with direct measurements. The best values of parameters are determined by minimizing the χ^2 value:

$$\sum_i \left[\frac{AP_i - (D_i - B_i)}{\sigma_i} \right]^2 = \min\,, \tag{1}$$

where the summation is done over all observations in which the telescope axis was pointed within 30° off the galactic center, A is the model normalization, P_i is the predicted count rate for a given detector in the i-th observation, D_i is the observed count rate in the 508 – 514-keV energy range, B_i is the predicted background count rate, and σ_i is the statistical error in the given observation. For a small number of counts in an individual observation ($N_i \leqslant 10-20$), the use of the simplest Poisson error $\sigma_i = \sqrt{N_i}$ frequently leads to the measurement and error correlation, as well as to a systematic shift in the parameter estimates [5]. To avoid this, errors were calculated from the known observation time using the mean values obtained from a large number of measurements. In the simplest model, it is assumed that the surface brightness is described by a two-dimensional Gaussian symmetrical relative to the Galactic Center. The normalization (the total flux) and width of the distribution were free model parameters. A slightly more flexible model includes an additional constant base defined as $AP_i + C$. Figure 2 depicts the total flux as a function of the Gaussian width for these two models and the dependence of $\chi^2 - \chi^2_{\min}$ [equation (1)] for the model with a constant base. The value of $\chi^2_{\min}$ equals 38,938 for 38,969 degrees of freedom (the number of individual measurements with the number of free parameters subtracted). As the signal-to-noise ratio is fairly low for individual observations, the small value of $\chi^2_{\min}$ is not a good indication of the consistency of data with the model, but rather indicates that the statistical measurement error was correctly estimated. Figure 2 implies that the best fit to observed data is achieved at a Gaussian width of around 6°. The total flux (the normalization of the Gaussian) therewith amounts to $\sim 7.6 \times 10^{-4}$ photons per s per cm^2 for the model with the base, and $\sim 10^{-3}$ photons per s per cm^2 for the model without the base. Such a difference in the radiant flux suggests a more complicated flux distribution than was assumed in these simple models. Nevertheless, the obtained value of flux reflects (to within a numerical factor on the order of unity) the total flux coming from the Galactic Center region. The precise value of this numerical coefficient depends on the assumed form of the surface brightness distribution.

Therefore, the data obtained by the INTEGRAL observatory demonstrate that the surface brightness of the central zone of the Galaxy is significantly higher than in any other direction, and the total flux from the central region reaches $\sim 10^{-3}$ photons per s per cm^2. More complex models [6, 7] for the 511-keV line surface brightness distribution, which, in particular, comprise a disk component and a central spheroidal part (bulge), lead to qualitatively similar conclusions that the radiant flux for the central component is appreciably higher than for the disk component. This conclusion is valid provided that the disk thickness is smaller than several dozen degrees.

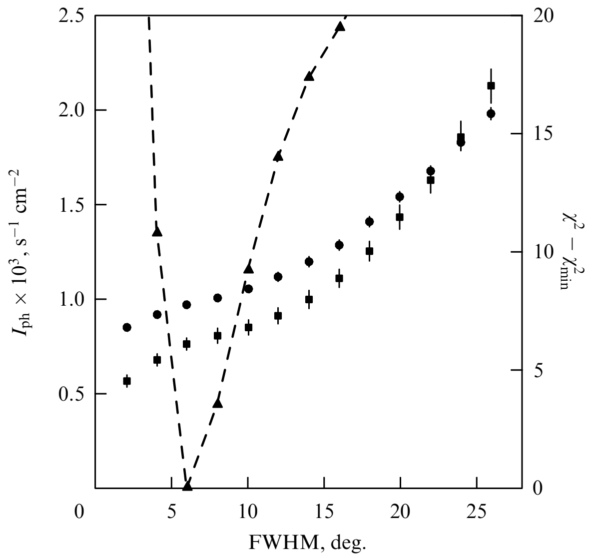

Figure 2. The flux $I_{\rm ph}$ in the energy range 508 – 514 keV as a function of the Gaussian width for two model surface brightness distributions: a two-dimensional Gaussian (circles), and a two-dimensional Gaussian plus a constant base (squares) . The dashed curve illustrates the dependence of the quantity $\chi - \chi^2_{\min}$ (the right axis) on the Gaussian width for the second model.

4. The spectrum of the 511-keV line emission

The data analysis in the 508 – 514-keV energy range, described in Section 3, was repeated for narrow 0.5-keV energy channels covering the range from 20 to 1000 keV. This allowed us to construct the spectrum [4] reflecting the dependence on the energy flux for a Gaussian width of 6°. This spectrum is presented in Fig. 3. The choice of the spatial model used — the Gaussian + constant (see Section 3) — is sufficiently conservative, as the inclusion of an additional free parameter decreases the statistical significance of the results, but allows the systematic noise to be suppressed. Another choice of the Gaussian width leads to changes in the spectrum normalization (see Fig. 2), but basic spectral parameters discussed in the present report are weakly dependent on the Gaussian width used. Table 1 lists parameters approximating the spectrum obtained. The spectral model includes the following components: a comparatively narrow Gaussian line (free parameters are the energy of the line center, the linewidth, and normalization), a three-photon continuum (free parameter is the normalization), and a power-law with a fixed photon index equal to 2.0. The power law was applied to take into account the hypothetical possibility that a broadband component (for example, diffuse nonthermal radiation from the interstellar medium near the galactic center) is present in the spectrum in addition to the annihilation emission. The ratio of fluxes in the first two components yields the fraction of annihilations due to positronium production:

$$F_{\mathrm{PS}} = \frac{2}{1.5 + 2.25\, F_{2\gamma}/F_{3\gamma}}\,, \tag{2}$$

where $F_{2\gamma}$ is the line flux, and $F_{3\gamma}$ is the three-photon continuum flux. The algebraic expression (2) directly follows from the assumption that ortho- and para-positroniums are formed in the ratio 3 : 1 and give rise to 3 and 2 photons during annihilation, respectively.

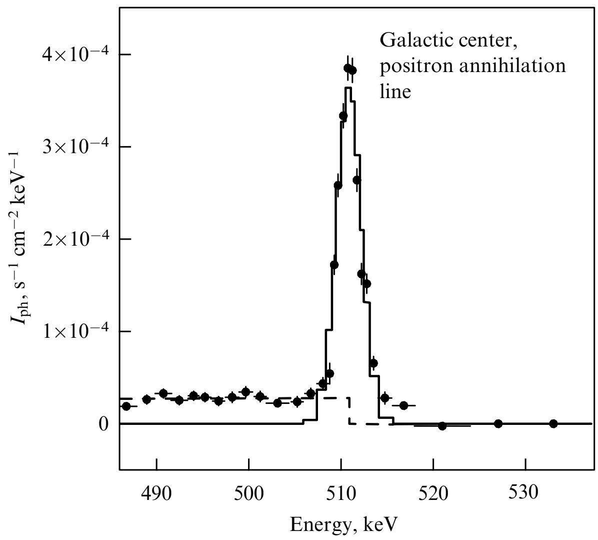

Figure 3. Annihilation emission spectrum from the central part of the Galaxy, obtained for one of the spatial model distributions of the galactic annihilation emission. Points show the three-photon decay contribution. The solid curve corresponds to the 511-keV line, while the dashed curve displays the three-photon continuum. The model curves presented have not been convolved with the instrumental energy resolution. The sharp edge of the three-photon continuum is actually smeared due to a finite resolution.

Table 1. Parameters of the spectral approximation of annihilation emission in the 450 – 550-keV range. The model includes a Gaussian line, an ortho-positronium continuum, and a power-law spectrum with a photon index equal to 2.0. Errors correspond to the 1σ confidence level for one parameter.

Parameter	Parameter value and error
E, keV	510.954 [510.88 – 511.03]
FWHM, keV	2.37 [2.12 – 2.62]
$F_{2\gamma} \times 10^4$ photons per s per cm^2	7.16 ± 0.36
$F_{3\gamma} \times 10^4$ photons per s per cm^2	26.1 ± 5.7
$F_{3\gamma}/F_{2\gamma}$	3.65 ± 0.82
F_{PS}	0.94 ± 0.06
χ^2 (number of degrees of freedom)	192.7 (193)

5. Constraints on the interstellar medium parameters

Two measurable quantities — the linewidth and the line-to-three-photon-continuum flux ratio — allow us to put restrictions on the temperature and degree of ionization of the medium where annihilation occurs. The positrons are assumed to be born 'hot', i.e., with energies above several hundred kiloelectron-volts. Then, the positrons slow down due to Coulomb losses in an ionized plasma or atomic photoionization and excitation in a neutral gas. Ultimately, the energy of the positrons becomes comparable to the temperature in the surrounding medium — a thermalization of positrons occurs. When the energy of the positrons decreases below several hundred electron-volts, the charge exchange with neutral atoms, photorecombination, or direct annihilation with free or bound electrons become effective (see, for example, Ref. [8]). In the analysis below we have considered a pure hydrogen gas without dust. To evaluate ionization, excitation, and charge exchange processes, we have used theoretical predictions by Kernoghan [9], which well fit with observations. For photorecombination and direct annihilation on free electrons, approximations from Ref. [10] have been adopted. The direct annihilation on bound electrons has been evaluated using approximations from Ref. [11]. For positrons slowing down during ionization of hydrogen atoms, it is necessary to specify the energy distribution of electrons in the final state. To this end we have made use of the final energy distribution obtained in the first Born approximation, and the normalization has been fixed to a value from Ref. [9]. For positrons slowing down by interacting with free electrons, we applied an analytical approximation [12] obtained for the energy loss by electrons. In the calculations we have assumed that during charge exchange and photorecombination ortho- and para-positroniums are produced according to their statistical weights, i.e., in the 3 : 1 ratio.

To trace the energy evolution of positrons and the formation of the annihilation emission spectra with due regard for all above processes, a Monte Carlo method has been applied. The emission spectrum produced by thermalized positrons with the Maxwellian energy distribution has been calculated separately. Estimates show that deviations from the Maxwellian distribution due to charge exchange of positrons with neutral atoms can be important at a plasma temperature of around 6000 K and a very low degree of ionization of less than 10^{-3}. For other combinations of the temperature and degree of ionization, deviations from the Maxwellian distribution are insignificant.

The annihilation line is predicted to have a form deviating from an ideal Gaussian and often shows the presence of both a broad and a narrow component. In that case, the linewidth traditionally defined as a 'full width at half maximum' is more sensitive to the narrow component, even if this component comprises a small fraction of the radiation. To avoid this, an effective linewidth has been calculated — the energy interval comprising 76% of the total line flux.

Results of the calculations are shown in Fig. 4, where each curve corresponds to a given temperature of the medium. The degree of ionization in the medium changes along the curves. It is easily seen that the curves presented in Fig. 4 form two families.

The first family of the curves corresponds to a gas with a temperature below ~ 6000 K. In a cold and neural medium, around 94% of positrons annihilate prior to the thermalization. The other 6% go below the positronium production threshold (6.8 eV) and then annihilate on bound electrons. The effective linewidth resulted from the positron annihilation with the positronium production is 5.3 keV. The annihilation on bound electrons yields an effective width of about 1.7 keV [13] due to the finite width of the velocity distribution of electrons bound in a hydrogen atom. The effective width (the sum of the broad and narrow components) of the line eventually formed is ~ 4.6 keV. If the degree of ionization in the medium exceeds $\sim 10^{-3}$, Coulomb losses become effective, i.e., the fraction of positrons that form positronium atoms prior to the thermalization decreases. For

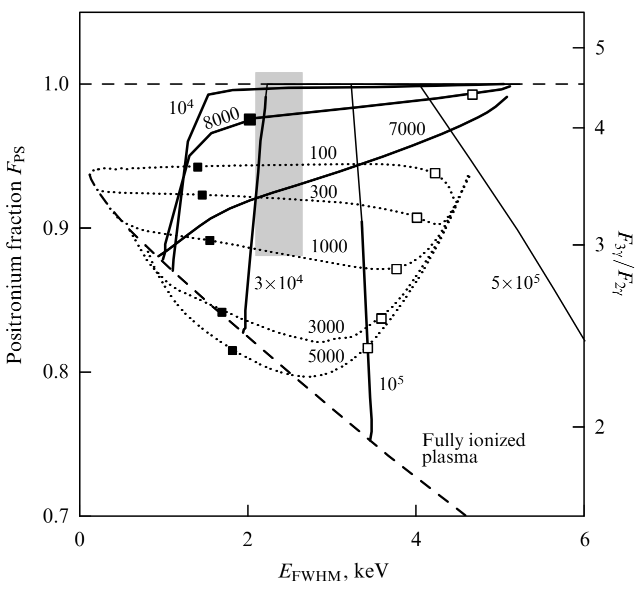

Figure 4. Effective width of the 511-keV line and annihilation fraction originating from the positronium production for different temperatures and degrees of ionization of the medium. The gray rectangle corresponds to parameter values compatible with the INTEGRAL observatory data. Theoretical curves are subdivided into two groups: low-temperature ($T < 5000$ K, dotted curves), and high-temperature ($T > 7000$ K, solid curves). The temperature is fixed for each curve (as shown in the figure), and the degree of ionization changes along the curve from 0 to 1. For low-temperature curves (and for the curve at $T = 8000$ K), the degree of ionization equal to 0.01 is marked with open squares, and the degree of ionization amounting up to 0.1 with full squares. The dashed curve is the fraction of the annihilation events due to the positronium production vs. the linewidth in a fully ionized medium.

positrons with energies below 6.8 eV, the most important are three processes: photorecombination with free electrons, and annihilation on both free and bound electrons. At the degree of ionization on the order of 10^{-2} and temperatures of about 1000 K, the annihilation on bound electrons decreases the fraction of positronium to 80–90%. If the degree of ionization is more than several percent, only photorecombination and annihilation on free electrons are significant, and both the fraction of positroniums and linewidth converge to the values as expected in a fully ionized plasma.

The second family of curves corresponds to temperatures above 7000 K. At such temperatures, thermalized positrons can produce positroniums in charge exchange reactions with hydrogen atoms. This process dominates over photorecombination and direct annihilation if the plasma is not highly ionized. Here, the fraction of positronium turns out to be very close to unity. Only for a significant degree of plasma ionization (on the order of 6–10% at $T = 8000$ K, and more at higher temperatures) does the annihilation on free electrons become important, and the positronium fraction starts decreasing with increasing degree of ionization (the almost vertical portions of the curves in Fig. 4).

The calculations illustrated in Fig. 4 have been performed for different combinations of temperatures and degrees of gas ionization, without regard to the viability of these combinations in real astrophysical conditions. For comparison, restrictions on the effective linewidth and positronium fraction as inferred from the INTEGRAL observations are shown in Fig. 4 by the gray rectangle. Clearly, two solutions are possible in terms of the one-phase medium: low-temperature ($T < 1000$ K), and high-temperature ($7000 < T < 4 \times 10^4$ K). Now we shall discuss the astrophysical aspect of these solutions.

According to the standard model for the interstellar medium [14, 15], there are several principal phases in the Galaxy: hot ($T > 10^5$ K), warm ($T \sim 8000$ K), and cold ($T < 100$ K).

It follows from Fig. 4 that a hot ($T > 10^5$ K) ionized medium cannot provide the dominant contribution to the observed annihilation emission spectrum. Indeed, the width of the line originated in such a medium is too large, and the positronium fraction is too low. The positronium fraction can be formally increased by decreasing the degree of gas ionization, but it is unlikely that in astrophysical conditions the degree of ionization can be made notably lower than in the purely collisional ionization equilibrium. A restriction on the contribution from a very hot ($T > 10^6$ K) fully ionized plasma can be obtained by adding a broad line to the model spectrum and finding the maximal line amplitude that would not contradict the observed spectrum within statistical errors. For example, the expected linewidth at $T = 10^6$ K equals ~ 11 keV [16], and such a line contribution is below 17% at the 90% confidence level. Assuming that the remaining photons ($< 83\%$) in the line are due to positronium annihilation and taking into account that at this temperature the direct annihilation and photorecombination rates are almost equal, we can conclude that less than 8% of the total positronium annihilations occur in a medium with temperature $T = 10^6$ K. Note that timescales for positron slowing down and annihilation in the interstellar medium depend both on the initial positron energy and on the medium properties (mainly on its density). The admissible time interval is fairly broad. For example, the mean time prior to annihilation at an initial positron energy of 0.5–1 MeV varies from 10 thousand to several hundred million years when passing from the cold phase to the hot phase. This means that positrons in the hot phase live sufficiently long, thus having time: (a) to leave the Galaxy or (b) to enter a denser phase and then annihilate. Consequently, a small fraction of annihilations in the hot medium is not by itself proof that positrons have not been produced in the hot medium.

A similar conclusion would also hold for a cold ($T < 10^3$ K) neutral medium. In this case, the expected positronium fraction is in agreement with observations, but

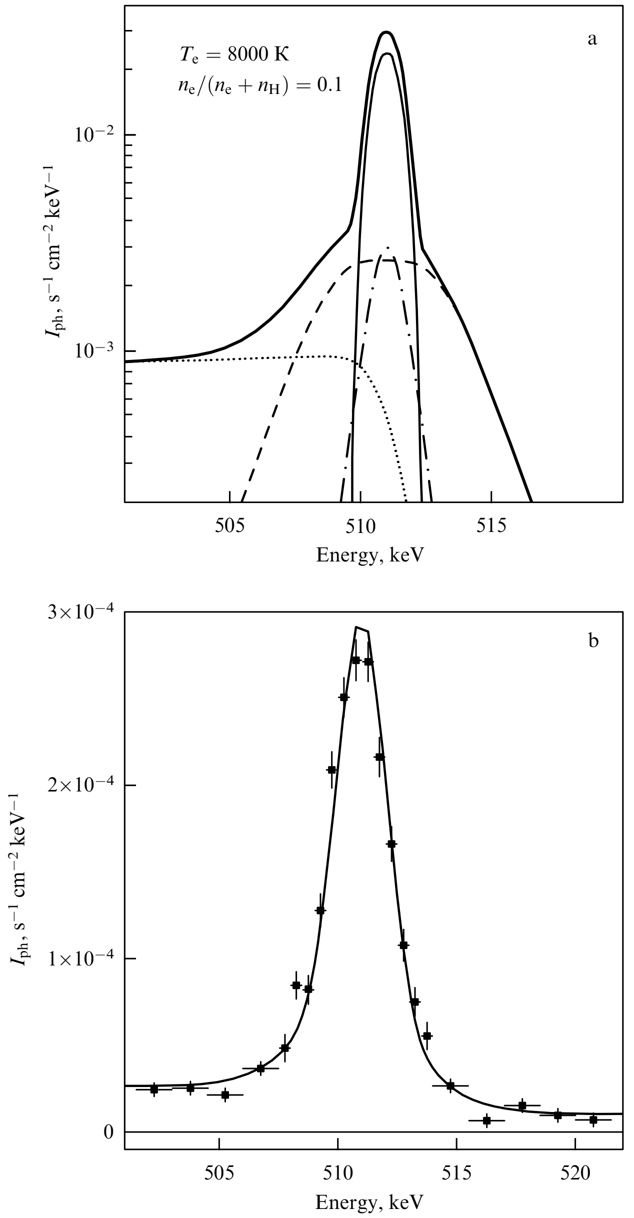

Figure 5. (a) Expected spectrum of the annihilation emission from a medium with temperature 8000 K and degree of ionization equal to 0.1. The dotted curve exhibits the contribution from a three-photon continuum; the dashed curve represents the annihilation line formed prior to thermalization of positrons; the thin solid curve corresponds to annihilation caused by production of para-positroniums after thermalizaiton, and the dot-and-dash line marks direct annihilation of thermalized positrons. The thick solid curve displays the complete annihilation emission spectrum. (b) Comparison of the model spectrum shown in figure (a) and convolved with instrumental energy resolution and the spectrum observed.

the expected linewidth of about 4.5 keV is too large. It is possible to reduce the linewidth by assuming a degree of ionization significantly higher than 10^{-2}. However, such an ionization degree for molecular and cold HI clouds is significantly higher than the typical values, which renders this solution improbable.

On the other hand, the degree of ionization in the warm ($T \sim 8000-10{,}000$ K) phase of the interstellar medium can vary from less than 0.1 to more than 0.8. Such a phase offers the possibility to explain the observed annihilation linewidths and positronium fractions in the spectrum. At temperatures 8000 – 10,000 K, the required degree of ionization amounts to a few percent. At a temperature of around 20,000 K, the necessary degree of ionization equals ~ 0.4. At temperatures above 30,000 K, plasma is virtually completely ionized, even if ionization by electron impact dominates. In typical astrophysical conditions, it is safe to assume that the degree of plasma ionization does not decrease below the value expected from collisional ionization by electrons. Possible photoionization additionally increases the ionization degree. Thus, the 'allowed' degree of ionization ranges from the collisional ionization value to unity. The corresponding portions of the curves in Fig. 4 are marked with the bold line.

Hence, Fig. 4 implies that the warm phase of the interstellar medium in the single-phase model provides the best fit with the spectrum observed. This conclusion is qualitatively consistent with the results [8] obtained from an analysis of earlier observations of annihilation emission. The detailed shape of the spectrum predicted by the annihilation model in a gas with temperature 8000 K and degree of ionization of 0.1 is demonstrated in Fig. 5a. The comparison of the model and observed spectra is shown in Fig. 5b.

It should be emphasized that although the single-phase model can reproduce observations quite well, more sophisticated models including annihilation in several phases [4] cannot be ruled out. The degree of phase ionization plays here a significant role. For example, the observations can be explained by assuming a presence of mixture of the cold neutral phase with a warm ionized phase in a 1:1 ratio. See papers [4, 17] for a more detailed analysis of this subject.

6. Discussion and conclusions

Observations made by INTEGRAL have provided the most precise current spectral measurements of the annihilation emission from positrons in the Galactic Center region.

The surface brightness of annihilation radiation is high in the central parts of the Galaxy (5 – 10 degrees in size), and is low in other parts. The flux from the central region amounts to $\sim 10^{-3}$ photons per s per cm^2. The uncertainty in this value is almost entirely related to that in the proposed surface brightness distribution. Assuming a distance of 8.5 kpc to the annihilation region and taking into account that the fraction of annihilations via positronium production is close to unity, we find that the observed flux corresponds to $\sim 2 \times 10^{43}$ annihilations of positrons per s. The corresponding luminosity is equal to $L_{e^+} \sim 1.6 \times 10^{37}$ erg s^{-1} (the number of positron annihilations times the positron rest energy). This puts serious energy restrictions on the positron production mechanism. For the initial positron Lorentz factor γ, the minimal expenditure of power is γL_{e^+}. If positrons originate from more energetic (or more massive) particles, the minimal power required to produce the necessary number of positrons can be estimated as

$$\frac{E_0}{m_e c^2}\, L_{e^+}\,,$$

where E_0 is the initial particle energy. For example, if positrons are produced by cosmic rays (via π^+-meson formation), the minimal expenditure of power equals $\approx 3\times 273\times L_{e^+}\approx 10^{40}$ erg s^{-1}. Here, we have taken into account that π^- and π^0 mesons are produced simultaneously with π^+ mesons. Decay of π^0 mesons must give rise to gamma emission at energies of 50 – 100 MeV with a luminosity on the order of 3×10^{39} erg s^{-1}. All these estimates, of course, have been obtained by assuming the stationarity of the annihilation emission.

An analysis of data gathered in the first series of observations indicates that the contribution from the disk component is smaller than the radiant flux from the central part of the Galaxy [6, 7]. The luminosity ratio is a model-dependent quantity strongly depending on the assumed properties of individual components, for example, on the disk component thickness.

The center of the line coincides with the rest energy of electrons (positrons) with high accuracy:

$$\frac{E}{m_e c^2} = 0.99991 \pm 0.00015\,.$$

Therefore, the mean line-of-sight velocity of the medium with reference to the Earth is no more than ~ 44 km s^{-1}. Observations of the annihilation linewidth also allow us to impose restrictions on the characteristic velocity of chaotic motions in the medium. The intrinsic linewidth in a medium at rest depends on the temperature and degree of its ionization (see Fig. 4) and can be sufficiently small ($\sim 1-1.5$ keV). Taking this into account, a conservative upper bound on the spread in the line-of-sight velocity amounts to ~ 800 km s^{-1}.

The combination of the observed linewidth (2.37 ± 0.25 keV) and positronium fraction ($F_{PS} = 0.96\pm 0.04$) can be explained by annihilation in a 'warm' phase of the interstellar medium with a characteristic temperature of around 8000 K and degree of its ionization on the order of 0.1. Annihilation in a single-phase cold ($T \leqslant 10^3$ K) or hot ($T \geqslant 10^5$ K) medium is inconsistent with the measurement data. However, a combination comprising several phases with different temperatures and degrees of ionization cannot also be excluded. The limit on the annihilation fraction in a very hot ($T \geqslant 10^6$ K) phase is below 8%.

The characteristics of the annihilation emission given above evidence against models of the positron origin in type II supernovae and massive stars, since such objects are found exclusively in the disk of the Galaxy and not in its bulge. Likewise (and from the energy consideration), a hypothesis for the production of positrons by interactions of cosmic rays with matter seems improbable. The INTEGRAL observatory data are more consistent with positron sources populating the Galactic bulge, in particular, with type Ia supernovae, low-mass binaries, or dark matter annihilation. Each of these mechanisms has its own advantages and shortcomings. One of the most important goals of continuing INTEGRAL observations is to impose more stringent constraints on the surface brightness distribution and spectral shape variations in the annihilation emission along and across the galactic plane. This will allow us to significantly narrow the class of physical processes mainly responsible for the production of positrons in the Galaxy.

References

1. Johnson W N (III), Harnden F R (Jr), Haymes R C *Astrophys. J.* **172** L1 (1972)
2. Leventhal M, MacCallum C J, Stang P D *Astrophys. J.* **225** L11 (1978)
3. Vedrenne G et al. *Astron. Astrophys.* **411** L63 (2003)
4. Churazov E et al. *Mon. Not. R. Astron. Soc.* **357** 1377 (2005)
5. Churazov E et al. *Astrophys. J.* **471** 673 (1996)
6. Teegarden B J et al. *Astrophys. J.* **621** 296 (2005)
7. Knödlseder J et al. *Astron. Astrophys.* **441** 513 (2005)
8. Bussard R W, Ramaty R, Drachman R J *Astrophys. J.* **228** 928 (1979)
9. Kernoghan A A et al. *J. Phys. B: At. Mol. Opt. Phys.* **29** 2089 (1996)
10. Gould R J *Astrophys. J.* **344** 232 (1989)
11. Bhatia A K, Drachman R J, Temkin A *Phys. Rev. A* **16** 1719 (1977)
12. Swartz W E, Nisbet J S, Green A E S *J. Geophys. Res.* **76** 8425 (1971)
13. Iwata K, Greaves R G, Surko C M *Phys. Rev. A* **55** 3586 (1997)
14. McKee C F, Ostriker J P *Astrophys. J.* **218** 148 (1977)
15. Kaplan S A, Pikel'ner S B *Fizika Mezhzvezdnoi Sredy* (Physics of Interstellar Medium) (Moscow: Nauka, 1979)
16. Crannell C J et al. *Astrophys. J.* **210** 582 (1976)
17. Jean P et al. *Astron. Astrophys.* **445** 579 (2006)

PACS numbers: **97.80.–d**, **98.70.–f**, 98.70.Qy
DOI: 10.1070/PU2006v049n03ABEH005970

Ultraluminous X-ray sources in galaxies — microquasars or intermediate mass black holes

S N Fabrika, P K Abolmasov, S V Karpov, O N Sholukhova, K K Ghosh

1. New class of X-ray sources

Ultraluminous X-ray sources (ULXs) in external galaxies were singled out in astrophysics as a new class of objects in 2000. Very bright X-ray sources had been discovered in galaxies earlier [1]. However, only after NASA's CHANDRA X-ray Observatory observations with a spatial resolution of $\approx 1''$ did it become clear that they constitute a new class of objects. These objects are not active galactic nuclei and not background quasars . In our report we briefly describe intriguing properties of these objects, basic models proposed for ULXs, and ideas that could help in understanding the nature of ULXs from analysis by observational methods. The last, in particular, includes studies of gaseous nebulae surrounding these objects, carried out on the 6-meter telescope of the Special Astrophysical Observatory (SAO) of RAS, as well as predictions of the specific X-ray spectra of ULXs.

ULXs are distinguished by their huge X-ray luminosities of $10^{39}-10^{42}$ egr s^{-1} in the 0.5 – 100 keV energy range. In our Galaxy, the maximum observed luminosities from accreting black holes in close binaries amount to $\sim 10^{38}$ erg s^{-1} in 'persistent' emission (i.e., not at the peak of an outburst). In this case, measured masses of the black holes fall within the range 4 – 15 solar masses. The total X-ray luminosity of a galaxy like our own or M31 ranges $(0.5-1)\times 10^{40}$ erg s^{-1} (2 – 20 keV). The critical luminosity of an accreting black can be estimated as

$$\frac{E_0}{m_e c^2} L_{e^+} ,$$

where E_0 is the initial particle energy. For example, if positrons are produced by cosmic rays (via π^+-meson formation), the minimal expenditure of power equals $\approx 3 \times 273 \times L_{e^+} \approx 10^{40}$ erg s^{-1}. Here, we have taken into account that π^- and π^0 mesons are produced simultaneously with π^+ mesons. Decay of π^0 mesons must give rise to gamma emission at energies of 50 – 100 MeV with a luminosity on the order of 3×10^{39} erg s^{-1}. All these estimates, of course, have been obtained by assuming the stationarity of the annihilation emission.

An analysis of data gathered in the first series of observations indicates that the contribution from the disk component is smaller than the radiant flux from the central part of the Galaxy [6, 7]. The luminosity ratio is a model-dependent quantity strongly depending on the assumed properties of individual components, for example, on the disk component thickness.

The center of the line coincides with the rest energy of electrons (positrons) with high accuracy:

$$\frac{E}{m_e c^2} = 0.99991 \pm 0.00015 .$$

Therefore, the mean line-of-sight velocity of the medium with reference to the Earth is no more than ~ 44 km s^{-1}. Observations of the annihilation linewidth also allow us to impose restrictions on the characteristic velocity of chaotic motions in the medium. The intrinsic linewidth in a medium at rest depends on the temperature and degree of its ionization (see Fig. 4) and can be sufficiently small ($\sim 1 – 1.5$ keV). Taking this into account, a conservative upper bound on the spread in the line-of-sight velocity amounts to ~ 800 km s^{-1}.

The combination of the observed linewidth (2.37 ± 0.25 keV) and positronium fraction ($F_{\mathrm{PS}} = 0.96 \pm 0.04$) can be explained by annihilation in a 'warm' phase of the interstellar medium with a characteristic temperature of around 8000 K and degree of its ionization on the order of 0.1. Annihilation in a single-phase cold ($T \leqslant 10^3$ K) or hot ($T \geqslant 10^5$ K) medium is inconsistent with the measurement data. However, a combination comprising several phases with different temperatures and degrees of ionization cannot also be excluded. The limit on the annihilation fraction in a very hot ($T \geqslant 10^6$ K) phase is below 8%.

The characteristics of the annihilation emission given above evidence against models of the positron origin in type II supernovae and massive stars, since such objects are found exclusively in the disk of the Galaxy and not in its bulge. Likewise (and from the energy consideration), a hypothesis for the production of positrons by interactions of cosmic rays with matter seems improbable. The INTEGRAL observatory data are more consistent with positron sources populating the Galactic bulge, in particular, with type Ia supernovae, low-mass binaries, or dark matter annihilation. Each of these mechanisms has its own advantages and shortcomings. One of the most important goals of continuing INTEGRAL observations is to impose more stringent constraints on the surface brightness distribution and spectral shape variations in the annihilation emission along and across the galactic plane. This will allow us to significantly narrow the class of physical processes mainly responsible for the production of positrons in the Galaxy.

References

1. Johnson W N (III), Harnden F R (Jr), Haymes R C *Astrophys. J.* **172** L1 (1972)
2. Leventhal M, MacCallum C J, Stang P D *Astrophys. J.* **225** L11 (1978)
3. Vedrenne G et al. *Astron. Astrophys.* **411** L63 (2003)
4. Churazov E et al. *Mon. Not. R. Astron. Soc.* **357** 1377 (2005)
5. Churazov E et al. *Astrophys. J.* **471** 673 (1996)
6. Teegarden B J et al. *Astrophys. J.* **621** 296 (2005)
7. Knödlseder J et al. *Astron. Astrophys.* **441** 513 (2005)
8. Bussard R W, Ramaty R, Drachman R J *Astrophys. J.* **228** 928 (1979)
9. Kernoghan A A et al. *J. Phys. B: At. Mol. Opt. Phys.* **29** 2089 (1996)
10. Gould R J *Astrophys. J.* **344** 232 (1989)
11. Bhatia A K, Drachman R J, Temkin A *Phys. Rev. A* **16** 1719 (1977)
12. Swartz W E, Nisbet J S, Green A E S *J. Geophys. Res.* **76** 8425 (1971)
13. Iwata K, Greaves R G, Surko C M *Phys. Rev. A* **55** 3586 (1997)
14. McKee C F, Ostriker J P *Astrophys. J.* **218** 148 (1977)
15. Kaplan S A, Pikel'ner S B *Fizika Mezhzvezdnoi Sredy* (Physics of Interstellar Medium) (Moscow: Nauka, 1979)
16. Crannell C J et al. *Astrophys. J.* **210** 582 (1976)
17. Jean P et al. *Astron. Astrophys.* **445** 579 (2006)

PACS numbers: **97.80.–d**, **98.70.–f**, 98.70.Qy
DOI: 10.1070/PU2006v049n03ABEH005970

Ultraluminous X-ray sources in galaxies — microquasars or intermediate mass black holes

S N Fabrika, P K Abolmasov, S V Karpov, O N Sholukhova, K K Ghosh

1. New class of X-ray sources

Ultraluminous X-ray sources (ULXs) in external galaxies were singled out in astrophysics as a new class of objects in 2000. Very bright X-ray sources had been discovered in galaxies earlier [1]. However, only after NASA's CHANDRA X-ray Observatory observations with a spatial resolution of $\approx 1''$ did it become clear that they constitute a new class of objects. These objects are not active galactic nuclei and not background quasars . In our report we briefly describe intriguing properties of these objects, basic models proposed for ULXs, and ideas that could help in understanding the nature of ULXs from analysis by observational methods. The last, in particular, includes studies of gaseous nebulae surrounding these objects, carried out on the 6-meter telescope of the Special Astrophysical Observatory (SAO) of RAS, as well as predictions of the specific X-ray spectra of ULXs.

ULXs are distinguished by their huge X-ray luminosities of $10^{39} – 10^{42}$ egr s^{-1} in the 0.5 – 100 keV energy range. In our Galaxy, the maximum observed luminosities from accreting black holes in close binaries amount to $\sim 10^{38}$ erg s^{-1} in 'persistent' emission (i.e., not at the peak of an outburst). In this case, measured masses of the black holes fall within the range 4 – 15 solar masses. The total X-ray luminosity of a galaxy like our own or M31 ranges $(0.5 - 1) \times 10^{40}$ erg s^{-1} (2 – 20 keV). The critical luminosity of an accreting black hole, or the Eddington luminosity at which radiation pressure is balanced by gravitational attraction of gas by the black hole, is $\approx 10^{38}$ erg s^{-1} for one solar mass, or $\approx 10^{39}$ erg s^{-1} for the 'typical' black hole mass. This implies that if radiation from ULXs is isotropic, their black hole masses can be as high as 10,000 solar masses.

X-ray emission from ULXs is strongly variable on time scales of a few dozen seconds to several years. No clear periodicities have been found, and yet quasiperiodic oscillations have been discovered [2] on time scales of ~ 20 s. Ultraluminous X-ray sources are distant objects registered in galaxies lying at distances of 3 Mpc and beyond, so searches for rapid brightness variability in ULXs have been restricted thus far by the sensitivity of X-ray observatories. The X-ray spectra of ULXs do not demonstrate pronounced spectral features; X-ray continuum is well fitted in average by a power-law $f_E \propto E^{-\alpha}$ with $\alpha = 0.5 - 2$, or by the so-called 'multicolor disk' (MCD) spectrum, which is defined as the spectrum of integral emission from a standard Shakura – Sunyaev accreting disk [3] with a temperature at the inner disk edge of $T_{\rm in} \sim 1-3$ keV. In this approximation, ULX spectra are quite similar to those of 'classical' stellar mass black holes, but the diversity of ULX spectra is fairly broad.

The principal property of ULXs is their location in star forming regions near galactic nuclei or in spiral arms of spiral or interacting galaxies. Studies on X-ray luminosity functions of galaxies [4] are in their infancy, however, it is already known that the number of X-ray sources in galaxies is proportional to the star formation rate. The frequency of ULXs (the bright end of the luminosity functions) is also determined by the star formation rate. A very crude estimate of the ULX frequency reduces to one object per ~ 20 spiral galaxies [5].

Clearly, ULXs are related to the young stellar population, i.e., to massive stars. Probably for this reason ULXs are frequently (or always) surrounded by gaseous nebulae. The nebulae around these objects have sizes from 10 to several hundred pc. Sometimes ULXs reside in the region of young star clusters. Clusters illuminate nebulae in sizes up to 300 – 400 pc, i.e., in this case large nebulae are genetically related to star clusters in which a ULX object emerged. Young (i.e., massive, bright and hot) stars not brighter than 20 – 22 stellar magnitudes are found within error boxes of these X-ray sources, so that the spectroscopy of these stars is difficult.

Presently, two models for ULXs are under consideration. According to the first model, ULXs represent supercritical accretion disks (SCADs) in binary systems with stellar mass black holes ($\sim 10M_\odot$), observed close to the disk axis [5, 6]. Black holes in binary systems that produce relativistic jets are called microquasars [7]. In this case, the real luminosity of a ULX can be much smaller: we observe X-ray radiation which is geometrically collimated in a funnel of SCAD and can also be relativistically amplified. The second model suggests that ULXs constitute 'intermediate' black holes, with masses between stellar values and those of supermassive black holes in galactic nuclei (IMBH, $10 - 10{,}000M_\odot$), surrounded by standard accretion disks [8, 9]. Assuming that a black hole has a large mass we broaden the allowed luminosity range. IMBHs are called missed class of astrophysical objects. In the most successful cosmological scenarios, supermassive stars with masses exceeding 100 solar masses must be formed at redshifts $z = 20-25$ ('the population III'). These stars should have left black holes that after the formation of galaxies were captured in galactic halos. Such black holes can accrete interstellar gas or capture stars in close orbits and are likely to be observed as ULXs [10]. Realistic estimates show that for luminosities as observed in ULXs the accretion rate of gas onto the black hole must be $\sim 10^{-6} M_\odot$ per year. In order for the interstellar gas accretion to proceed, the surrounding conditions for an IMBH must be very specific. For IMBH to capture a donor star, the latter would have to be a massive star. Any of these conditions sharply decreases the frequency of IMBH seen as ULXs.

Here, we argue in favor of the first model for ULXs, especially because such X-ray sources in galaxies were predicted [5] from studies of the galactic object SS 433. This is a unique object in the Galaxy comprising a close binary system with a black hole $\sim 10M_\odot$ persistently accreting gas with a highly supercritical rate [7, 11, 12]. The evolution stage of the donor in SS 433 (mass loss on the 'thermal time scale') is very short, $10^4 - 10^5$ years, which explains the rarity of such objects. The orientation of the SS 433 system is such that the observer cannot 'look' into the supercritical accretion disk funnel. In paper [5], we discussed observational appearances of SS 433 type objects (more precisely, of SS 433 itself) seen close to the disk and relativistic jet axis and concluded that such objects can form a new class of extragalactic X-ray sources. We continue to develop the idea that ULXs are supercritical accretion disks like SS 433, viewed under favorable orientation. In what follows we shall describe two crucial experiments: (1) observations of nebulae around ULXs and their comparison to the nebula around SS 433; in contrast to stars, extended nebulae turn out to be quite bright at megaparsec distances; analysis of emission lines of the nebulae allows fairly reliable diagnostics of the gas ionization source, and (2) the study of possible properties of the funnel in a supercritical accretion disk, enabling the prediction of the X-ray spectrum of ULXs.

2. Nebulae surrounding ULXs and SS 433

SS 433 is surrounded by an elongated radio nebula W 50 produced by the interaction of SS 433's jets with the ambient interstellar medium [13]. The nebula emits synchrotron radiation and relativistic electrons appear due to a deceleration of jets. At the jet deceleration sites ($\sim \pm 50$ pc from the center), bright optical filaments emitting hydrogen lines and forbidden lines of sulfur, nitrogen, and oxygen are observed. The filamentary structure expands with a velocity of about 50 km s^{-1}. Nebulae around ULXs, studied by us, have similar sizes and luminosities in emission lines, and almost the same total energetics ranging $10^{51} - 10^{52}$ erg [14].

In Figure 1 we present maps of the MF 16 nebula surrounding the ULX in the galaxy NGC 6946 as obtained by observations with the 6-meter telescope BTA SAO RAS. The multipupil field spectrograph (MPFS) [15] with an angular resolution of $1''$ has been used. In the [OIII] lines, a velocity gradient along the nebula in the East – West direction was discovered. More detailed later observations carried out with the SCORPIO spectrograph [17] revealed that the velocity variation along the nebula (its size is around 20 pc) reaches 100 km s^{-1}.

Figure 2 demonstrates the results of observations by the same instrument of the nebula surrounding ULX-1 in the galaxy IC 342. We also detected a velocity gradient (overall expansion of the nebula) equal to ± 20 km s^{-1}. This nebula is fairly dim as the light from the galaxy IC 342 itself is strongly absorbed by dust in the Milky Way.

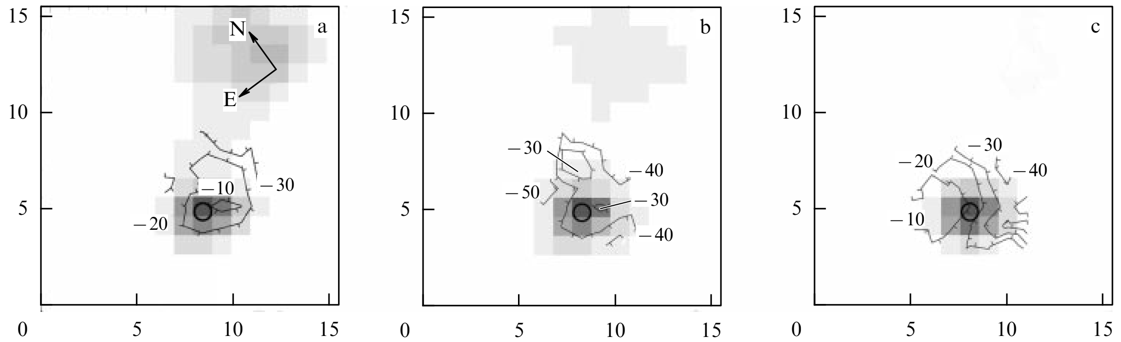

Figure 1. Results of integral-field spectroscopy of the nebula MF 16 surrounding a ULX in the galaxy NGC 6946. Maps of 15″ × 15″ regions in Hα (a), [SII] λ 6717, 6734 (b), and [OIII] λ 4959, 5007 (c) lines are presented. The circle marks the position of the X-ray source as observed by the CHANDRA X-ray Observatory. Lines of equal radial velocities (in units [km s^{-1}]) are shown. The lines' hatches indicate the direction of the radial velocity gradient.

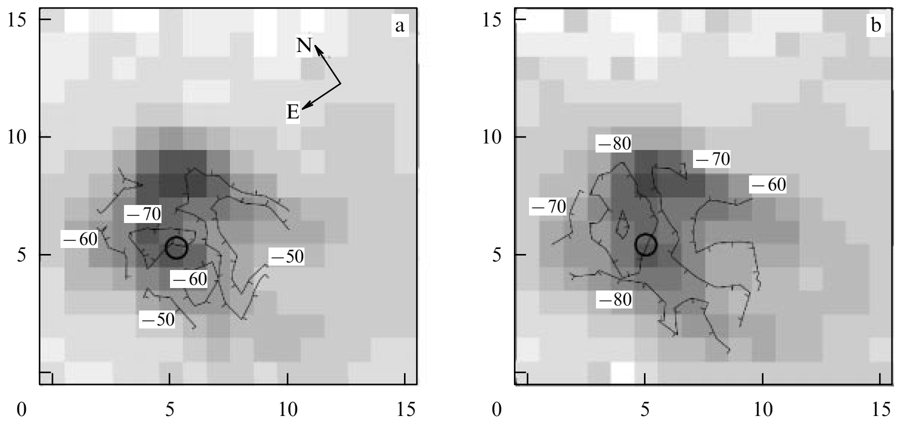

Figure 2. Integral-field spectroscopy of the nebula surrounding ULX-1 in the galaxy IC 342. Maps in Hα (a) and [SiII] λ 6717, 6734 (b) lines are shown. Other notations as in Fig. 1.

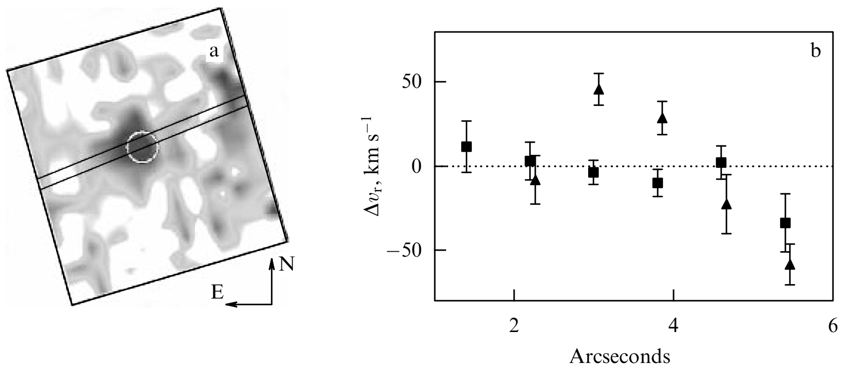

Figure 3. Integral-field spectroscopy of the nebula surrounding a ULX in the Holmberg II galaxy. (a) Map in the HeII λ 4686 line; two straight lines mark the position of the spectrograph slits. (b) The radial velocity difference in this line and in the [OIII] line measured along the nebula [18]; squares and triangles correspond to the upper and lower slit, respectively.

In Fig. 3 we present the results of observations by the same instrument of the nebula surrounding a ULX in the galaxy Holmberg II. A velocity gradient of ±50 km s^{-1} was also discovered on scales of ±50 pc [18]. The velocity along the nebula was measured in more detail by the BTA slit spectrograph.

In all three nebulae we observed, the intensity ratios of the diagnostic lines testify to collisional gas ionization (by shocks). Two additional conclusions directly relating to the physics of the central source are as follows.

(1) The gas velocity gradients of 50 – 100 km s^{-1} on scales of 20 – 100 pc suggest dynamically disturbed nebulae. An IMBH cannot disturb gas on such scales, as the Bondi capture radius is no more than 0.1 pc. In addition, these nebulae are too large and energetic to fit standard relations for supernova remnants. These nebulae are very likely to be powered by the central object via jet activity, as in the case of SS 433 galactic object.

(2) An additional source of hard UV radiation is necessary to explain the luminosity in high-excitation lines and the line spectrum. The luminosity of this source ($\sim 10^{40}$ erg s^{-1}) is as high as the X-ray luminosity.

In Fig. 4, we present images of the three nebulae at the same linear scale. Ring-like structures are visible on high-

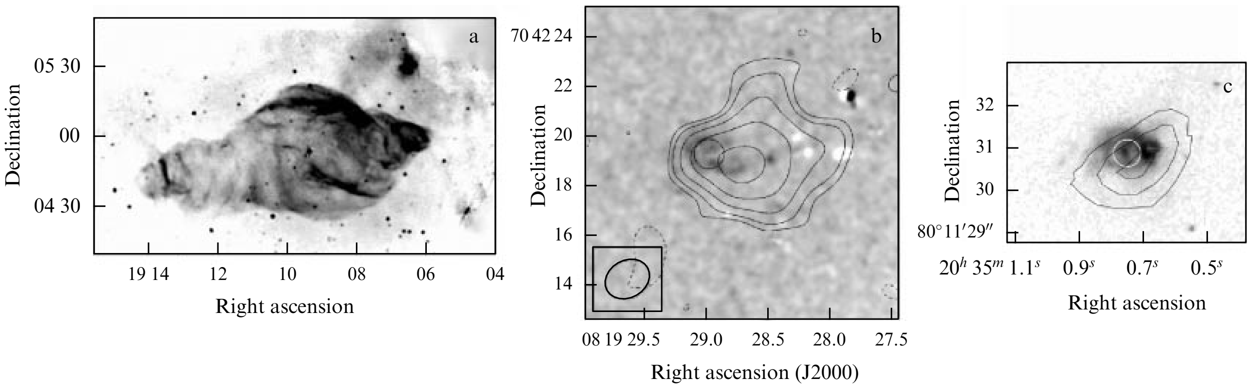

Figure 4. Three nebulae at the same spatial scale. (a) Image of the W 50 nebula [13] with SS 433 in the center, obtained by the VLA radio telescope. (b) Image of the nebula around the Holmberg II ULX, obtained by the HST space telescope in the HeII line with radio isophotes from the VLA radio telescope [24]. (c) The MF 16 nebula in lines Hα+[SII], surrounding the NGC 6946 ULX imaged by HST with the VLA radio isophotes [26]. The CHANDRA observations of X-ray source positions are shown by circles.

resolution images of nebulae in galaxies Holmberg II and NGC 6946, taken in spectral lines by the space telescope. In both cases, (spatially unresolved) radio sources are shifted toward the brightest ring-like structure. According to our data [14, 18], in both cases the part of the nebula coinciding with the radio source moves to the observer. One can imagine that these two nebulae around ULXs are similar to the W 50 nebula surrounding SS 433, and yet with the principal axis close ($i = 10° - 30°$) to the line of sight. We should continue observations to obtain a more reliable sample of nebulae around ULXs.

3. The structure of the funnel in SS 433, X-ray luminosities and spectra of ULXs

We start by briefly describing basic parameters of SS 433 [7] and possible structure of the funnel of the supercritical accretion disk in this system. The persistent and significantly supercritical rate of gas accretion on a black hole ($\sim 10 M_\odot$) is the main feature of SS 433 that makes it distinct from other known X-ray binaries. This leads to the formation of a supercritical accretion disk and relativistic jets. In contrast to jets in other microquasars, which are launched only during outbursts, jets in SS 433 are permanent and 'heavy', i.e., they consist of ordinary gas. The velocity of the jets is virtually constant and reaches 0.26 of the speed of light.

The SS 433 system is observed close to the accretion disk plane, i.e., we cannot view the bottom or internal walls of the funnel. A very bright UV source with $L \sim 10^{40}$ erg s^{-1} and temperature $T = (5-7) \times 10^4$ K [19, 20] is observed, located nearly at the site where relativistic jets appear from beneath a photosphere in the accretion disk wind. The wind mass loss rate equals $\dot{M}_{\rm w} \sim 10^{-5}\, M_\odot$ per year. The optical jets in SS 433 ($\sim 10^{15}$ cm) consist of small dense gas clouds. Both the optical and X-ray jets are strongly collimated ($\sim 1°$). The observed X-ray radiation is formed in X-ray jets being cooled ($\sim 10^{12}$ cm) and the X-ray luminosity is $\sim 10^4$ times smaller than the UV luminosity of the object. However, the 'kinetic luminosity' of the jets is very high: $L_{\rm k} \sim 10^{39}$ erg s^{-1}.

Jets in SS 433 are produced in the supercritical disk funnel. Most likely, the funnel's interior is formed in a thick accretion disk, and the funnel's exterior continues in the dense wind from the disk. Figure 5 schematically shows the funnel. The black square represents the region a few hundred Schwarzschild radii in size, inside which numerical simulations can be performed at present. Two-dimensional hydrodynamical calculations of supercritical accretion disks, accounting for radiation [21, 22], demonstrate that a broad funnel with a total opening angle $\theta_f \approx 40° - 50°$ is formed close to the center. The funnel walls are dynamical. Outside the funnel, convection is important in the inner parts of the disk.

Assuming a luminosity in the funnel to be on the order of the total one in SS 433 [5, 23] and adopting funnel's opening angle obtained from numerical calculations, we can find the 'observed' X-ray luminosity from the funnel in SS 433 to be $L_{\rm X} \sim 10^{41}$ erg s^{-1}, and the expected occurrence rate of such objects ~ 0.1 per Milky Way type galaxy.

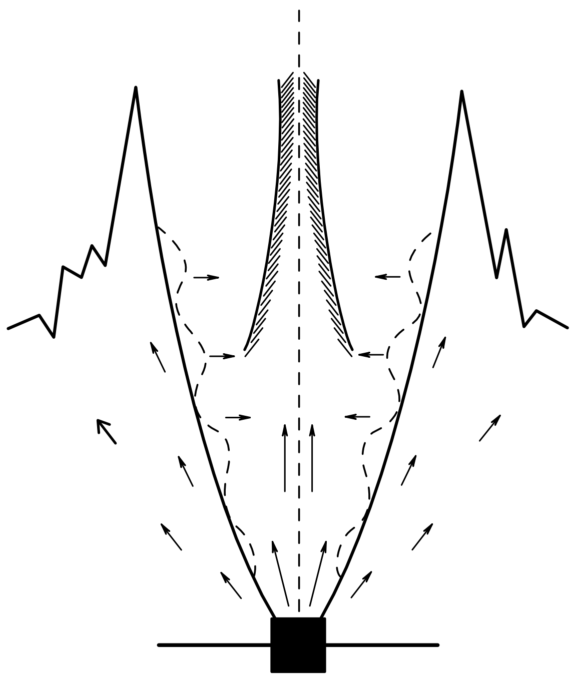

Figure 5. Schematic of the funnel in the supercritical accretion disk in SS 433. The thick curve outlines the funnel photosphere. Shown are the slow wind from the disk (~ 1000 km s^{-1}) and the fast wind inside the funnel that is collimated into a jet at the funnel's outlet.

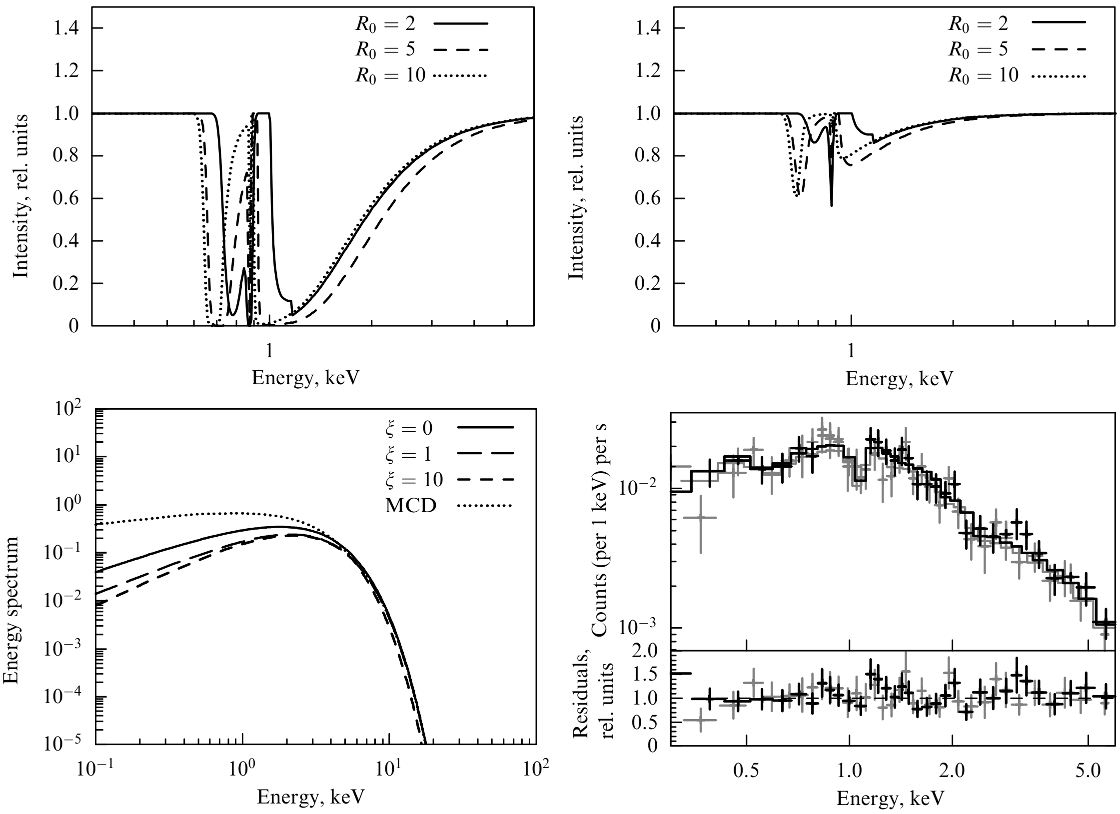

Figure 6. Expected X-ray spectra from the funnel in SS 433. The continuum spectrum (bottom left) is calculated for different radiation-to-gas pressure ratios ξ in the deepest parts of the funnel. Profiles of the OVIII blend of the Lα and Lc transitions for different efficiencies of gas acceleration by jets are shown for optically thick (top left) and optically thin (top right) cases. The gas acceleration starts at $R_0 = 1$ (photosphere of funnel's bottom) and ends at $R_0 = 2, 5, 10$. The bottom right panel shows the spectrum of a ULX in the NGC 4736 galaxy obtained by the XMM-Newton X-ray Observatory.

On the other hand, the critical luminosity of a black hole with mass $10\,M_\odot$ equals $L_{\rm edd} \sim 10^{39}$ erg s^{-1}. At a strongly supercritical accretion rate in SS 433 of $\dot M/\dot M_{\rm cr} \sim 10^3$, the total disk luminosity exceeds the critical one [3] by $(1 + \ln(\dot M/\dot M_{\rm cr})) \sim 10$ times. The second factor (relativistic beaming) only mildly increases the observed luminosity, $1/(1-\beta)^{2+\alpha} \sim 2.5$, where $\beta = V_{\rm j}/c = 0.26$ is the jet velocity in SS 433, and α is the X-ray spectral index. The third factor (collimation of radiation by the funnel) is also geometrical, and for the funnel's opening angle $\theta_{\rm f} \approx 40^\circ - 50^\circ$ it amounts to $\Omega_{\rm f}/2\pi \sim 10$. It is seen that the observed (apparent) luminosity from the supercritical disk can amount to $L_{\rm X} \sim 2 \times 10^{41}$ erg s^{-1}, which is consistent with what is observed from ULXs.

To estimate the emerging X-ray spectrum from the funnel, we developed in paper [23] a simplified funnel model (MCF, 'multicolor funnel'). The temperature of the funnel walls was calculated for two limiting cases of the gas temperature in the opaque wind outside the walls: when the gas pressure dominates $[T(r) \propto r^{-1}]$ or when the radiation pressure dominates $[T(r) \propto r^{-1/2}]$. From observations we can infer the temperature of the external funnel photosphere and the funnel's depth (the photospheric level at the bottom is calculated from the known mass loss in the jets). The temperature of the deepest funnel walls available for observations was estimated to fall within the range $1 \times 10^6 - 1.7 \times 10^7$ K.

Figure 6 portrays X-ray spectra of the funnel in the MCF model, calculated for different values of the radiation-to-gas pressure ratio $\xi = aT_0^3/3k_{\rm B}n_0$ in the deepest parts of funnel walls. The temperature of these parts is taken to be $T_0 = 1$ keV. We also plot the X-ray spectrum calculated for the multitemperature disk model MCD ($T_{\rm inn} = 1$ keV), which fits the observed hard spectra of ULX best. Clearly, our MCF model can also explain ULX spectra.

The jet velocity in SS 433 ($0.26c$) and its surprising stability enables one to assume that the line-locking effect [25] is important for acceleration of jets in the funnel. An absorption spectrum with Lc- and Kc-breaks of hydrogen-like and helium-like ions can be emitted by the inner walls of the funnel. The MCF model predicts a very complex absorption spectrum consisting of Kα/Kc and Lα/Lc blends of the most abundant heavy elements.

In Fig. 6, we also plot the calculated profiles of the line OVIII of transitions Lα and Lc. The observed spectrum from ULX in NGC 4736 galaxy as obtained by the XMM-Newton X-ray Observatory is also plotted; different lines show two spectra taken simultaneously by two spectrometers. The residuals obtained after dividing the observed spectrum by a model power-law spectrum with an absorption feature at 1.03 keV are shown. Unfortunately, the spectral resolution of the existing X-ray observatories (and small fluxes from ULXs) do not allow detailed investigation of absorption spectra.

The model for the supercritical accretion disk funnel predicts a very complex X-ray absorption spectrum from a ULX, consisting of blends from transitions Lα/Lc, Kα/Kc of the most abundant elements. Variations of physical parameters of gas in the funnel [velocity, density, temperature, filling factor (jet collimation), etc.] can strongly complicate the spectrum. Observations of X-ray spectra with high signal-to-noise ratios are required to study such absorption spectra. Nevertheless, the predicted spectral complexity, as well as the dependence of line profiles on the funnel structure, and the gas acceleration and collimation in the funnel, provide remarkable possibilities for direct observational probing of the supercritical accretion disk funnels and relativistic jet formation mechanisms.

We conclude that observations of nebulae surrounding ULXs directly suggest that ULXs are likely to be SS 433 type microquasars and not intermediate mass black holes. Observations of X-ray spectra of ULXs by upcoming new-generation X-ray observatories, which will start operating in a few years, may uncover the intricate spectra of ULXs formed in funnels of supercritical accretion disks around stellar mass black holes.

References

1. Fabbiano G, in *The Hot Universe*: *Proc. of the 188th Symp. of the Intern. Astronomical Union, Kyoto, Japan, August 26–30, 1997* (Eds K Koyama, S Kitamoto, M Itoh) (Dordrecht: Kluwer Acad. Publ., 1998) p. 93
2. Strohmayer T E, Mushotzky R F *Astrophys. J.* **586** L61 (2003)
3. Shakura N I, Sunyaev R A *Astron. Astrophys.* **24** 337 (1973)
4. Grimm H-J, Gilfanov M, Sunyaev R *Astron. Astrophys.* **391** 923 (2002)
5. Fabrika S, Meshcheryakov A, in *Galaxies and their Constituents at the Highest Angular Resolutions*: *IAU Symp. 205*: *Proc. of the 24th General Assembly of the IAU, Manchester, United Kingdom, 15–18 August, 2000* (Eds R T Schilizzi et al.) (San Francisco, Calif.: Astron. Soc. of the Pacific, 2001) p. 268
6. King A R et al. *Astrophys. J. Lett.* **552** L109 (2001)
7. Fabrika S *Astrophys. Space Phys. Rev.* **12** 1 (2004)
8. Colbert E J M, Mushotzky R F *Astrophys. J.* **519** 89 (1999)
9. Miller J M, Fabian A C, Miller M C *Astrophys. J. Lett.* **614** L117 (2004)
10. Madau P, Rees M J *Astrophys. J.* **551** L27 (2001)
11. Margon B *Annu. Rev. Astron. Astrophys.* **22** 507 (1984)
12. Cherepashchuk A *Space Sci. Rev.* **102** 23 (2002)
13. Dubner G M et al. *Astron. J.* **116** 1842 (1998)
14. Fabrika S, Abolmasov P, Sholukhova O (2006) (in preparation)
15. Afanasiev V L, Dodonov S N, Moiseev A V, in *Stellar Dynamics*: *from Classic to Modern*: *Proc. of the Intern. Conf., Saint Petersburg, August 21–27, 2000* (Eds L P Ossipkov, I I Nikiforov) (Saint Petersburg: Saint Petersburg Univ., Sobolev Astron. Institute, 2001) p. 103
16. Abolmasov P, Fabrika S, Sholukhova O (2006) (in preparation)
17. Afanas'ev V L, Moiseev A V *Pis'ma Astron. Zh.* **31** 214 (2005) [*Astron. Lett.* **31** 194 (2005)]
18. Lehmann I et al. *Astron. Astrophys.* **431** 847 (2005)
19. Cherepashchuk A M, Aslanov A A, Kornilov V G *Astron. Zh.* **59** 1157 (1982) [*Sov. Astron.* **26** 697 (1982)]
20. Dolan J F et al. *Astron. Astrophys.* **327** 648 (1997)
21. Eggum G E, Coroniti F V, Katz J I *Astrophys. J. Lett.* **298** L41 (1985)
22. Okuda T et al. *Mon. Not. R. Astron. Soc.* **357** 295 (2005)
23. Fabrika S, Karpov S (2006) (in preparation)
24. Miller N A, Mushotzky R F, Neff S G *Astrophys. J. Lett.* **623** L109 (2005)
25. Shapiro P R, Milgrom M, Rees M J *Astrophys. J. Suppl. Ser.* **60** 393 (1986)
26. van Dyk S D et al. *Astrophys. J. Lett.* **425** L77 (1994)